

## Chemical Diversity in Three Massive Young Stellar Objects associated with 6.7 GHz CH<sub>3</sub>OH Masers

KOTOMI TANIGUCHI,<sup>1,2,\*</sup> MASAO SAITO,<sup>3,1</sup> LITON MAJUMDAR,<sup>4</sup> TOMOMI SHIMOIKURA,<sup>5</sup> KAZUHITO DOBASHI,<sup>5</sup>  
HIROYUKI OZEKI,<sup>6</sup> FUMITAKA NAKAMURA,<sup>3,1</sup> TOMOYA HIROTA,<sup>3,1</sup> TETSUHIRO MINAMIDANI,<sup>2,1</sup> YUSUKE MIYAMOTO,<sup>2,†</sup> AND  
HIROYUKI KANEKO<sup>2</sup>

<sup>1</sup>*Department of Astronomical Science, School of Physical Science, SOKENDAI (The Graduate University for Advanced Studies), Osawa, Mitaka, Tokyo 181-8588, Japan*

<sup>2</sup>*Nobeyama Radio Observatory, National Astronomical Observatory of Japan, Minamimaki, Minamisaku, Nagano 384-1305, Japan*

<sup>3</sup>*National Astronomical Observatory of Japan, Osawa, Mitaka, Tokyo 181-8588, Japan*

<sup>4</sup>*Jet Propulsion Laboratory, California Institute of Technology, 4800 Oak Grove Drive, Pasadena, CA 91109, USA*

<sup>5</sup>*Department of Astronomy and Earth Sciences, Tokyo Gakugei University, Nukukitamachi, Koganei, Tokyo 184-8501, Japan*

<sup>6</sup>*Department of Environmental Science, Faculty of Science, Toho University, Miyama, Funabashi, Chiba 274-8510, Japan*

(Received; Revised; Accepted)

Submitted to ApJ

### ABSTRACT

We have carried out observations in the 42–46 and 82–103 GHz bands with the Nobeyama 45-m radio telescope, and in the 338.2–339.2 and 348.45–349.45 GHz bands with the ASTE 10-m telescope toward three high-mass star-forming regions containing massive young stellar objects (MYSOs), G12.89+0.49, G16.86–2.16, and G28.28–0.36. We have detected HC<sub>3</sub>N including its <sup>13</sup>C and D isotopologues, CH<sub>3</sub>OH, CH<sub>3</sub>CCH, and several complex organic molecules (COMs). Combining our previous results of HC<sub>5</sub>N in these sources, we compare the  $N(\text{HC}_5\text{N})/N(\text{CH}_3\text{OH})$  ratios in the three observed sources. The ratio in G28.28–0.36 is derived to be  $0.091^{+0.109}_{-0.039}$ , which is higher than that in G12.89+0.49 by one order of magnitude, and that in G16.86–2.16 by a factor of  $\sim 5$ . We investigate the relationship between the  $N(\text{HC}_5\text{N})/N(\text{CH}_3\text{OH})$  ratio and the  $N(\text{CH}_3\text{CCH})/N(\text{CH}_3\text{OH})$  ratio. The relationships of the two column density ratios in G28.28–0.36 and G16.86–2.16 are similar to each other, while HC<sub>5</sub>N is less abundant when compared to CH<sub>3</sub>CCH in G12.89+0.49. These results imply a chemical diversity in the lukewarm ( $T \sim 20 - 30$  K) envelope around MYSOs. Besides, several spectral lines from complex organic molecules, including very-high-excitation energy lines, have been detected toward G12.89+0.49, while the line density is significantly low in G28.28–0.36. These results suggest that organic-poor MYSOs are surrounded by a carbon-chain-rich lukewarm envelope (G28.28–0.36), while organic-rich MYSOs, namely hot cores, are surrounded by a CH<sub>3</sub>OH-rich lukewarm envelope (G12.89+0.49 and G16.86–2.16).

*Keywords:* astrochemistry — ISM: molecules — stars: formation — stars: massive

### 1. INTRODUCTION

Molecules are a unique and powerful tool in astronomy. They provide an excellent diagnosis of the physical conditions and processes in the regions where they reside. Progress in this field called astrochemistry is mainly driven by observations from various single-dish and interferometers at millimeter/sub-millimeter wavelengths along with space telescopes at mid- and far-infrared wavelengths (e.g., van Dishoeck 2017).

Unsaturated carbon-chain molecules tend to be abundant in young low-mass starless cores and deficient in low-mass star-forming cores (Suzuki et al. 1992; Hirota et al. 2009), because they are mainly formed from ionized carbon (C<sup>+</sup>)

Corresponding author: Kotomi Taniguchi  
kotomi.taniguchi@nao.ac.jp

\* Research Fellow of Japan Society for the Promotion of Science

Present address: National Astronomical Observatory of Japan, Osawa, Mitaka, Tokyo 181-8588, Japan

† Present address: National Astronomical Observatory of Japan, Osawa, Mitaka, Tokyo 181-8588, Japan

and atomic carbon (C) via ion-molecule reactions in the early stage of molecular clouds and destroyed mainly by reaction with oxygen atoms and depleted onto dust grains in the late stage. Carbon-chain molecules have been found to be abundant around two low-mass protostars; IRAS 04368+2557 in L1527 (Sakai et al. 2008) and IRAS 15398–3359 in Lupus (Sakai et al. 2009a). In these protostars, carbon-chain molecules are newly formed from CH<sub>4</sub> evaporated from dust grains in the lukewarm ( $T \sim 20 - 30$  K) gas (Sakai et al. 2008). Such a carbon-chain chemistry around the low-mass protostars was named warm carbon chain chemistry (WCCC, Sakai et al. 2008). The difference between hot corino chemistry and WCCC is considered to be brought by the different timescale of the starless core phase; the long and short starless core phases lead to hot corino and WCCC sources, respectively (Sakai et al. 2008). Recently, sources possessing both hot corino and WCCC characteristics have been found and high-spatial-resolution observations showed that the spatial distributions of carbon-chain molecules and COMs are different with each other (e.g., Imai et al. 2016).

Saturated complex organic molecules (COMs), organic species consisting of more than six atoms and being rich in hydrogen (Herbst & van Dishoeck 2009), are classically known to be abundant in the dense and hot ( $n > 10^6$  cm<sup>-3</sup>,  $T \geq 100$  K) gas around young stellar objects (YSOs). Besides, COMs also have been found in the gas phase before ice thermally evaporates at temperatures above 100 K (Vastel et al. 2014). At these low temperatures, COMs can be desorbed from icy grain mantles via different types of non-thermal desorption process such as: (1) the cosmic-ray desorption mechanism (Reboussin et al. 2014), (2) the chemical desorption mechanism (desorption due to the exothermicity of surface reactions; Garrod et al. 2007), and (3) the photo-desorption (Ruaud et al. 2016). Role of barrier-less gas phase reactions to form COMs was also proposed recently by Balucani et al. (2015). Recent observations show the presence of some COMs, methylformate (HCOOCH<sub>3</sub>), dimethyl ether (CH<sub>3</sub>OCH<sub>3</sub>), and methyl cyanide (CH<sub>3</sub>CN), and the complex radical methoxy (CH<sub>3</sub>O) in regions where the dust temperature is less than 30 K; pre-stellar cores (Bacmann et al. 2012; Vastel et al. 2014; Potapov et al. 2016) and cold envelopes of low-mass protostars (Öberg et al. 2010; Cernicharo et al. 2012; Jaber et al. 2014). Grain-surface chemistry certainly plays a role, for example in forming hydrogenated species during the prestellar phase (Tielens & Hagen 1982; Caselli & Ceccarelli 2012), but not necessarily in the formation of all COMs.

Not only in the low-mass star-forming regions, new questions arise in the chemistry around massive young stellar objects (MYSOs). Fayolle et al. (2015) compared the chemistry between organic-poor MYSOs and organic-rich MYSOs, namely hot cores. They suggested that hot cores are not required to form COMs and temperature and initial ice composition possibly affect complex organic distributions around MYSOs. Green et al. (2014) detected HC<sub>5</sub>N, the second shortest cyanopolynes (HC<sub>2n+1</sub>N,  $n = 1, 2, 3, \dots$ ), in 35 hot cores associated with the 6.7 GHz methanol masers, which give us the exact positions of MYSOs (Urquhart et al. 2013). However, there remained the possibility that the emission of HC<sub>5</sub>N comes from the outer cold molecular clouds or other molecular clouds in the large single-dish beam ( $\sim 0.95'$ ). Taniguchi et al. (2017b) carried out observations toward four MYSOs where Green et al. (2014) detected HC<sub>5</sub>N, using the Green Bank 100-m telescope (GBT) and the Nobeyama 45-m radio telescope. The four target sources were selected adding three criteria mentioned in Section 2 and we chose three sources showing the highest HC<sub>5</sub>N peak intensities (G12.89+0.49, G16.86–2.16, and G28.28–0.36) and a source showing the low HC<sub>5</sub>N peak intensity with the high CH<sub>3</sub>CN peak intensities (G10.30–0.15). They detected the high-excitation-energy ( $E_u/k \sim 100$  K) lines of HC<sub>5</sub>N, which cannot be detected if HC<sub>5</sub>N exists in the cold dark clouds, in the three sources (G12.89+0.49, G16.86–2.16, and G28.28–0.36) and confirmed that HC<sub>5</sub>N exists in the warm gas around MYSOs. Therefore, carbon-chain molecules seem to be formed in the lukewarm gas around MYSOs, as well as WCCC sources in the low-mass star-forming regions. At the present stage, we do not know the relationships between carbon-chain molecules and COMs around MYSOs.

In this paper, we report the observational results in the 42–46, 82–103, 338.2–339.2 and 348.45–349.45 GHz bands obtained with the Nobeyama 45-m radio telescope and the Atacama Submillimeter Telescope Experiment (ASTE) 10-m telescope toward three MYSOs, G12.89+0.49, G16.86–2.16, and G28.28–0.36. We derive the rotational temperatures and beam-averaged column densities of HC<sub>3</sub>N, CH<sub>3</sub>OH, and CH<sub>3</sub>CCH (Section 4). We compare the spectra and the chemical composition among the three sources, combining with previous HC<sub>5</sub>N data (Taniguchi et al. 2017b), in order to investigate the relationship between carbon-chain species and COMs in high-mass star-forming regions (Section 5).

## 2. OBSERVATIONS

The observations presented in this paper were conducted in the Nobeyama 45-m radio telescope and the ASTE joint observation program (Proposal ID: JO161001, PI: Kotomi Taniguchi, 2016-2017 season). The observing parameters of each frequency band are summarized in Table 1. The Nobeyama 45-m telescope data have been partly published in Taniguchi et al. (2017b).

**Table 1.** Observing parameters

Frequency (GHz)	Telescope	Beam size ( $''$ )	$\eta_{\text{mb}}$ (%)	$T_{\text{sys}}$ (K)	$\Delta\nu$ (kHz)	$T_{\text{rms}}^{\text{a}}$ (mK)
42–46	Nobeyama	37	71	120–150	122.07	6–14
82–103	Nobeyama	18 <sup>b</sup>	54 <sup>b</sup>	120–200	244.14	3–6
338–349.4	ASTE	22	60	300–700	1000	16–24

<sup>a</sup>In  $T_{\text{A}}^*$  scale.

<sup>b</sup>The values are at the 86 GHz.

**Table 2.** Properties of our target sources

Source	R.A. <sup>a</sup>	Decl. <sup>a</sup>	$D$ (kpc)	$V_{\text{LSR}}^{\text{a}}$ (km s <sup>-1</sup> )	Other Association <sup>b</sup>	
	(J2000)	(J2000)			UCH II <sup>a</sup>	outflow
G12.89+0.49	18 <sup>h</sup> 11 <sup>m</sup> 51 <sup>s</sup> .4	-17 <sup>o</sup> 31'30''	2.50 <sup>c</sup>	33.3	N	Y <sup>d</sup>
G16.86–2.16	18 <sup>h</sup> 29 <sup>m</sup> 24 <sup>s</sup> .4	-15 <sup>o</sup> 16'04''	1.67 <sup>d</sup>	17.8	N	Y <sup>d</sup>
G28.28–0.36	18 <sup>h</sup> 44 <sup>m</sup> 13 <sup>s</sup> .3	-04 <sup>o</sup> 18'03''	3.0 <sup>e</sup>	48.9	Y	Y <sup>f</sup>

<sup>a</sup>Purcell et al. (2006)

<sup>b</sup>The symbols of “Y” and “N” represent detection and non-detection, respectively. “UCH II” indicates an ultracompact H II region lying within a radius of 19''. The 6.7 GHz methanol masers are associated with all of the four sources.

<sup>c</sup>Reid et al. (2014)

<sup>d</sup>Li et al. (2016)

<sup>e</sup>Green et al. (2014)

<sup>f</sup>Cyganowski et al. (2008)

The source selection criteria were described in Taniguchi et al. (2017b) as follows:

1. The source declination is above  $-21^\circ$ ,
2. the distance ( $D$ ) is within 3 kpc, and
3. CH<sub>3</sub>CN was detected ( $\int T_{\text{mb}} dv > 0.5$  K km s<sup>-1</sup> for  $J_K = 5_0 - 4_0$  line, Purcell et al. 2006).

Eight sources in the HC<sub>5</sub>N-detected source list of Green et al. (2014) meet the above three criteria. We chose three sources among the eight selected sources which show the highest peak intensities of HC<sub>5</sub>N ( $T_{\text{mb}} > 120$  mK). Table 2 summarizes the properties of our three target sources. The observed positions correspond to the 6.7 GHz methanol maser positions, which show exact positions of the MYSOs (Urquhart et al. 2013).

### 2.1. Observations with the Nobeyama 45-m Radio Telescope

We carried out observations with the Nobeyama 45-m radio telescope from 2017 January to March. We employed the position-switching mode. The integration time was 20 seconds per on-source and off-source positions. The on-source positions are summarized in Table 2 and the off-source positions were set to be +15' away in declination. The total integration time is  $\sim 1$  hr and 2–4.5 hr in the 42–46 GHz and 82–103 GHz band observations, respectively.

The Z45 receiver (Nakamura et al. 2015) and the TZ receiver (Nakajima et al. 2013) were used in the observations at 42–46 GHz and 82–103 GHz, respectively. The main beam efficiency ( $\eta_{\text{mb}}$ ) and the beam size (HPBW) at 43GHz

were 71% and  $37''$ , respectively. The main beam efficiency and the beam size at 86 GHz were 54% and  $18''$ , respectively. The system temperatures were 120–150 K and 120–200 K during the observations at 42–46 GHz and 82–103 GHz, respectively. We used the SAM45 FX-type digital correlator (Kamazaki et al. 2012) in frequency settings whose bandwidths and resolutions are 500 MHz and 122.07 kHz for the Z45 observations, and 1000 MHz and 244.14 kHz for the TZ observations, respectively. The frequency resolutions correspond to the velocity resolution of  $\sim 0.85 \text{ km s}^{-1}$ .

The telescope pointing was checked every 1.5 hr by observing the SiO maser line ( $J = 1 - 0$ ; 43.12203 GHz) from OH39.7+1.5 at  $(\alpha_{2000}, \delta_{2000}) = (18^{\text{h}}56^{\text{m}}03^{\text{s}}.88, +06^{\circ}38'49''.8)$ . We used the Z45 receiver for the pointing check during the 42–46 GHz band observations and the H40 receiver for the pointing check during the 82–103 GHz band observations. The pointing error was less than  $3''$ .

The rms noises are 6–14 and 3–6 mK in  $T_{\text{A}}^*$  scale in the 42–46 GHz and 82–103 GHz bands, respectively. The baseline was fitted with a linear function. The absolute flux calibration error is approximately 10%.

### 2.2. Observations with the ASTE 10-m Telescope

The observations with the ASTE 10-m telescope were conducted in 2016 September and October. The DASH345 receiver and the WHSF FX-type digital spectrometer (Iguchi & Okuda 2008; Okuda & Iguchi 2008) were used. The observed frequency ranges are 338.2–339.2 and 348.45–349.45 GHz. The main beam efficiency and beam size were 60% and  $22''$ , respectively. The system temperatures were between 300 and 700 K, depending on the elevation and weather conditions. The frequency setting was 2048 MHz bandwidth and 1 MHz frequency resolution. The frequency resolution corresponds to  $0.86 \text{ km s}^{-1}$ , which is almost equal to that of observations with the Nobeyama 45-m telescope. The total integration time is approximately 1–2.5 hr, which is different among sources.

We checked the telescope pointing every 2 hr by observing the  $^{12}\text{CO}$  ( $J = 3 - 2$ ) line from W Aql at  $(\alpha_{2000}, \delta_{2000}) = (19^{\text{h}}15^{\text{m}}23^{\text{s}}.35, -07^{\circ}02'50''.3)$ . The pointing error was less than  $2''$ .

The rms noise levels in the line-free regions are 23–24, 19–20, and 16–17 mK in  $T_{\text{A}}^*$  scale in G12.89+0.49, G16.86–2.16, and G28.28–0.36, respectively. Some scans were excluded due to bad baselines. A linear fit was applied for baseline subtraction. The absolute flux calibration error is approximately 10%.

## 3. RESULTS

We conducted data reduction using the Java Newstar software, an astronomical data analyzing system of the Nobeyama 45-m telescope and the ASTE 10-m telescope.

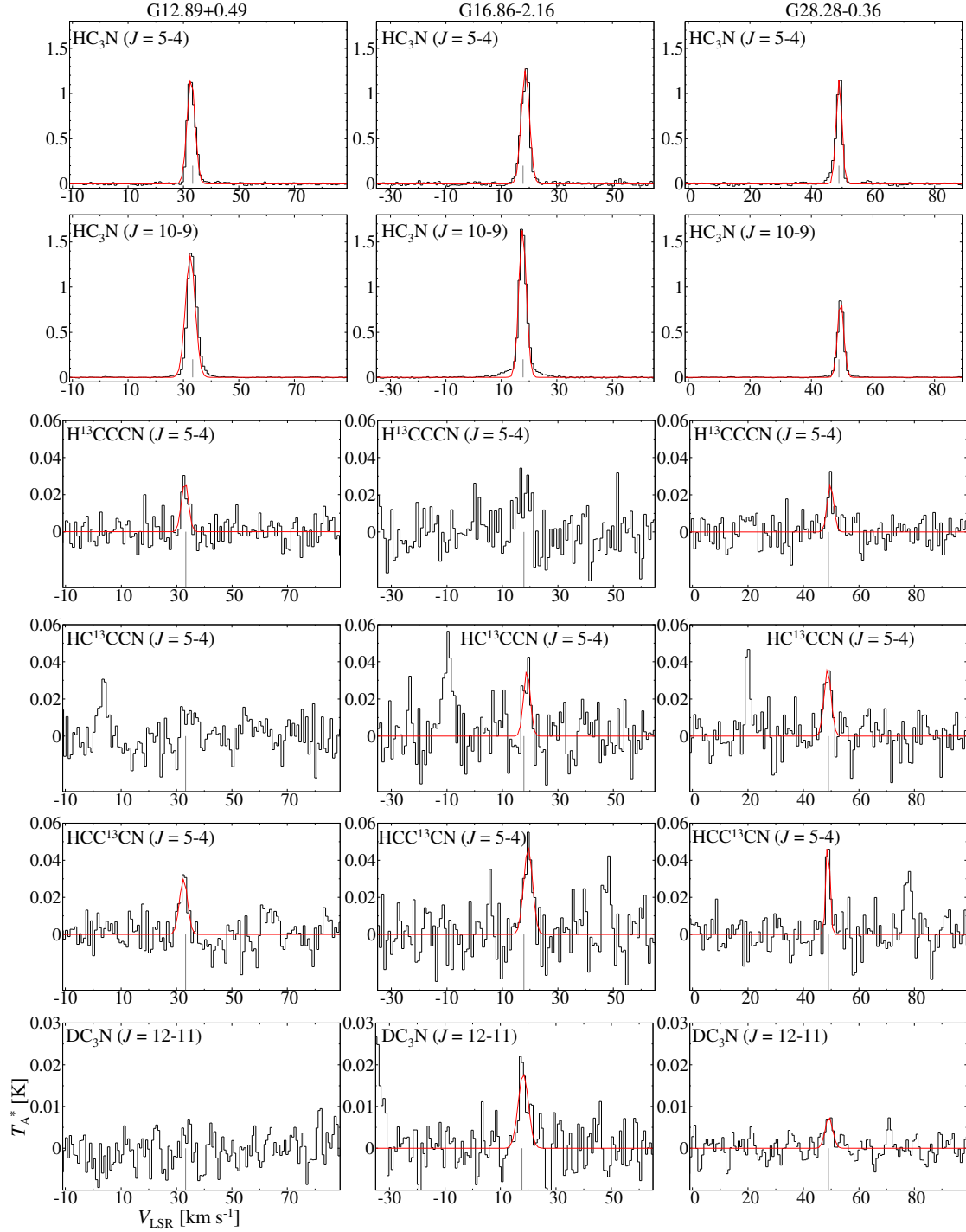
### 3.1. Observational Results with the Nobeyama 45-m Radio Telescope

Figure 1 shows the spectra of the main isotopologue  $\text{HC}_3\text{N}$  and its  $^{13}\text{C}$  and D isotopologues in the three sources obtained with the Nobeyama 45-m radio telescope. We fitted the spectra with a Gaussian function and obtained the spectral line parameters as summarized in Table 3. Two rotational transitions,  $J = 5 - 4$  and  $10 - 9$ , of the main isotopologue are in the observed frequency bands, and they were detected from all of the three sources. Its three  $^{13}\text{C}$  isotopologues have been detected from G28.28–0.36 with a signal-to-noise (S/N) ratio above 4.  $\text{HC}^{13}\text{CCN}$  was not detected in G12.89+0.49, whereas  $\text{H}^{13}\text{CCCN}$  was not detected in G16.86–2.16.  $\text{DC}_3\text{N}$  was detected in G28.28–0.36 with a S/N ratio of 3 and in G16.86–2.16 with a S/N ratio above 4. The  $V_{\text{LSR}}$  values agree with the systemic velocities of each source (Table 2).

The line profiles of the main isotopologue show wing emission, suggesting that  $\text{HC}_3\text{N}$  also exists in the molecular outflow (e.g., Shimajiri et al. 2015; Taniguchi et al. 2018). Such wing emission is most prominent in G16.86–2.16, where the blue and red components are clearly detected. The red and blue components are prominent in G12.89+0.49 and G28.28–0.36, respectively. These features of wing emission of  $\text{HC}_3\text{N}$  are similar to those of  $\text{CH}_3\text{OH}$  (Figure 3), as mentioned later. Hence, the origin of molecular outflows is plausible.

Figure 2 shows the spectra of  $\text{CH}_3\text{CCH}$  obtained with the Nobeyama 45-m radio telescope. Its  $J = 5 - 4$  and  $6 - 5$   $K$ -ladder lines ( $K = 0 - 0, 1 - 1, 2 - 2, \text{ and } 3 - 3$ ) were detected from the three sources with a S/N ratio above 4. We fitted the spectra with four-component Gaussian profiles. We fixed the centroid velocities to be the systemic velocities for each source (Table 2). The spectral line parameters are summarized in Table 4. There is no presence of wing emission in the  $\text{CH}_3\text{CCH}$  spectra and the lines are well fitted with the Gaussian profile.

Nine thermal  $\text{CH}_3\text{OH}$  lines were detected from G12.89+0.49, and eight lines, except for  $6_{-2,5} - 7_{-1,7}$   $E$  transition, were detected from the other two sources with a S/N ratio above 4 as shown in Figure 3. We fitted the spectra with Gaussian profiles and the spectral line parameters are summarized in Table 5. For the four lines shown in the top



**Figure 1.** Spectra of the main isotopologue  $\text{HC}_3\text{N}$  and its  $^{13}\text{C}$  and D isotopologues in the three sources. The red lines show the Gaussian fitting results and gray vertical lines show the systemic velocity for each source.

**Table 3.** Spectral line parameters of the main isotopologue HC<sub>3</sub>N and its <sup>13</sup>C and D isotopologues in the three sources with the Nobeyama 45-m telescope

Species	Frequency <sup>a</sup>	$E_u/k$	G12.89+0.49				G16.86−2.16				G28.28−0.36			
			$T_{\text{mb}}$	FWHM	$\int T_{\text{mb}} dv$	$V_{\text{LSR}}^b$	$T_{\text{mb}}$	FWHM	$\int T_{\text{mb}} dv$	$V_{\text{LSR}}^b$	$T_{\text{mb}}$	FWHM	$\int T_{\text{mb}} dv$	$V_{\text{LSR}}^b$
Transition	(GHz)	(K)	(K)	(km s <sup>−1</sup> )	(K km s <sup>−1</sup> )	(km s <sup>−1</sup> )	(K)	(km s <sup>−1</sup> )	(K km s <sup>−1</sup> )	(km s <sup>−1</sup> )	(K)	(km s <sup>−1</sup> )	(K km s <sup>−1</sup> )	(km s <sup>−1</sup> )
HC <sub>3</sub> N														
$J = 5 - 4$	45.490314	6.5	1.64 (4)	3.35 (9)	5.8 (2)	32.8	1.76 (5)	3.50 (12)	6.6 (3)	18.7	1.62 (6)	2.22 (10)	3.8 (2)	49.0
$J = 10 - 9$	90.979023	24.0	2.58 (12)	4.1 (2)	11.3 (8)	32.5	3.15 (7)	3.22 (8)	10.8 (4)	17.7	1.64 (3)	2.39 (5)	4.16 (11)	49.5
H <sup>13</sup> CCCN														
$J = 5 - 4$	44.084172	6.4	0.037 (7)	3.0 (7)	0.12 (4)	33.0	< 0.036	...	...	...	0.036 (6)	2.7 (5)	0.10 (3)	49.8
HC <sup>13</sup> CCN														
$J = 5 - 4$	45.2973345	6.5	< 0.027	...	...	...	0.050 (12)	2.8 (8)	0.15 (6)	18.9	0.051 (8)	3.0 (6)	0.16 (4)	48.7
HCC <sup>13</sup> CN														
$J = 5 - 4$	45.3017069	6.5	0.042 (7)	3.4 (7)	0.15 (4)	32.5	0.090 (13)	3.7 (6)	0.36 (8)	19.3	0.073 (13)	1.7 (4)	0.13 (4)	48.8
DC <sub>3</sub> N														
$J = 12 - 11$	101.314818	31.6	< 0.013	...	...	...	0.034 (6)	4.3 (9)	0.16 (4)	18.2	0.014 (3)	3.2 (7)	0.049 (13)	49.2

TANIGUCHI ET AL.

NOTE—Numbers in the parentheses are the standard deviation of the Gaussian fit, expressed in units of the last significant digits. For example, 1.64 (4) means  $1.64 \pm 0.04$ . The upper limits correspond to the  $3\sigma$  limits.

<sup>a</sup> Taken from the Cologne Database for Molecular Spectroscopy (CDMS; Müller et al. 2005).

<sup>b</sup> The errors are  $0.85 \text{ km s}^{-1}$ , which corresponds to the velocity resolution (Section 2.1).

**Table 4.** Spectral line parameters of CH<sub>3</sub>CCH in the three sources with the Nobeyama 45-m telescope

Transition	Frequency <sup>a</sup> (GHz)	$E_u/k$ (K)	G12.89+0.49			G16.86−2.16			G28.28−0.36		
			$T_{\text{mb}}$ (K)	FWHM (km s <sup>−1</sup> )	$\int T_{\text{mb}} dv$ (K km s <sup>−1</sup> )	$T_{\text{mb}}$ (K)	FWHM (km s <sup>−1</sup> )	$\int T_{\text{mb}} dv$ (K km s <sup>−1</sup> )	$T_{\text{mb}}$ (K)	FWHM (km s <sup>−1</sup> )	$\int T_{\text{mb}} dv$ (K km s <sup>−1</sup> )
<i>J</i> = 5 − 4											
<i>K</i> = 0 − 0	85.4573003	12.3	0.958 (14)	3.03 (5)	3.09 (6)	0.616 (18)	3.18 (9)	2.08 (8)	0.638 (14)	2.19 (5)	1.49 (4)
<i>K</i> = 1 − 1	85.4556667	19.5	0.785 (14)	3.20 (6)	2.67 (7)	0.496 (18)	3.02 (11)	1.59 (8)	0.477 (13)	2.46 (7)	1.25 (5)
<i>K</i> = 2 − 2	85.4507663	41.2	0.324 (14)	3.08 (13)	1.06 (6)	0.190 (19)	2.8 (3)	0.57 (8)	0.160 (13)	2.44 (19)	0.42 (5)
<i>K</i> = 3 − 3	85.4426012	77.3	0.168 (14)	3.2 (3)	0.56 (7)	0.065 (16)	3.9 (9)	0.27 (9)	0.044 (13)	2.6 (7)	0.12 (5)
<i>J</i> = 6 − 5											
<i>K</i> = 0 − 0	102.5479844	17.2	1.741 (13)	3.51 (3)	6.50 (8)	1.079 (14)	3.07 (5)	3.53 (7)	0.791 (12)	2.16 (4)	1.82 (4)
<i>K</i> = 1 − 1	102.5460242	24.5	1.412 (13)	3.81 (4)	5.72 (8)	0.845 (13)	3.26 (6)	2.93 (7)	0.676 (12)	2.09 (4)	1.50 (4)
<i>K</i> = 2 − 2	102.5401446	46.1	0.637 (13)	3.75 (9)	2.54 (8)	0.385 (13)	3.19 (13)	1.31 (7)	0.239 (12)	2.09 (12)	0.53 (4)
<i>K</i> = 3 − 3	102.5303476	82.3	0.374 (13)	3.61 (14)	1.44 (8)	0.192 (14)	3.0 (2)	0.61 (7)	0.086 (13)	1.8 (3)	0.16 (4)

NOTE—Numbers in the parentheses are the standard deviation of the Gaussian fit, expressed in units of the last significant digits.

<sup>a</sup>Taken from the Cologne Database for Molecular Spectroscopy (CDMS; Müller et al. 2005).



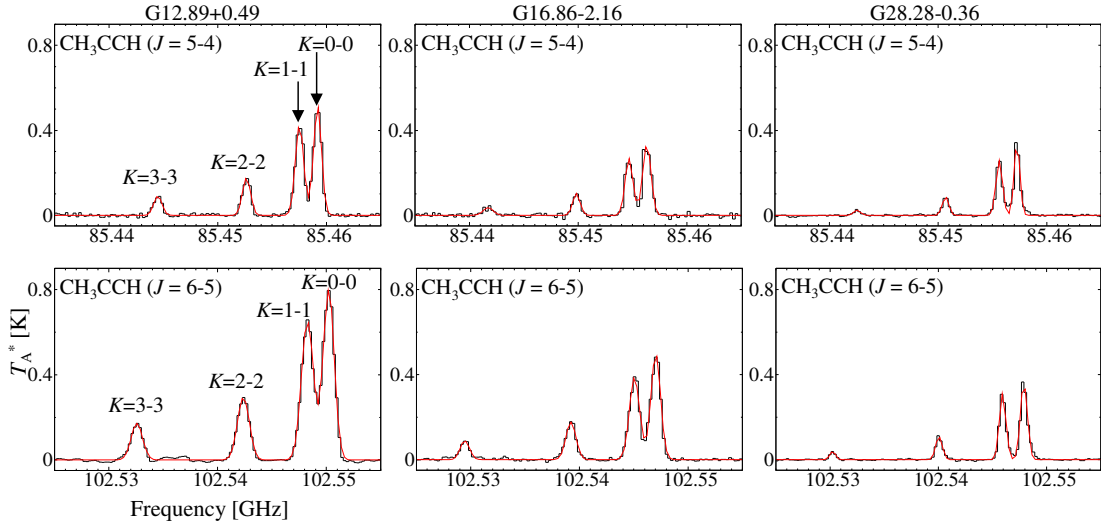


**Figure 2.** Spectra of  $\text{CH}_3\text{CCH}$  in the three sources. The red lines show the Gaussian fitting results.

panels of Figure 3, we applied the four-component Gaussian fitting. In the same way as for  $\text{CH}_3\text{CCH}$ , the centroid velocities were fixed to be the systemic velocities of each source (Table 2). The wing emission for red and blue velocity components are seen in G16.86–2.16, while only the red component is found in G12.89+0.49. In G28.28–0.36, no wing emission is seen, which may be due to their lower line intensities.

Figures 4 and 5 show the spectra in the frequency bands covered with the TZ receiver. Several lines from COMs have been detected with a S/N ratio above 4. An analysis of the COMs requires the simultaneous fitting of multiple species to avoid blending effects with other lines. In our case, detected COMs have similar excitation-energy and such fitting cannot degenerate excitation temperatures and column densities. Therefore, we cannot derive their rotational temperatures and column densities accurately and we will not discuss COMs in the rest of this paper. We summarize the detection and non-detection of COMs in each source in Table 6. G12.89+0.49 is the most line-rich source with strong peak intensities, and both nitrogen-bearing COMs and oxygen-bearing COMs have been detected. On the other hand, only  $\text{CH}_3\text{OH}$  and  $\text{CH}_3\text{CHO}$  were detected with weak peak intensities in G28.28–0.36.

### 3.2. Observational Results with the ASTE 10-m Telescope

Figure 6 shows the spectra in the 338.2–339.2 and 348.45–349.45 GHz bands obtained with the ASTE 10-m telescope. Table 7 summarizes the spectral line parameters obtained from the Gaussian fitting. The detection limit was set at a S/N ratio above 4. The  $V_{\text{LSR}}$  values are consistent with the systemic velocities of each source (Table 2)<sup>1</sup>. Several high-excitation energy ( $E_u/k > 200$  K) lines from  $\text{CH}_3\text{OH}$  and  $\text{CH}_3\text{CN}$  were detected from G12.89+0.49. On the other hand, only two lower-excitation energy ( $E_u/k < 75$  K) lines of  $\text{CH}_3\text{OH}$  and  $\text{CCH}$  were detected from G28.28–0.36. The line density in G16.86–2.16 is between those in G12.89+0.49 and G28.28–0.36. The relatively high-excitation energy line of  $\text{CH}_3\text{OH}$  ( $7_{4,3} - 6_{4,2} A^+$  transition;  $E_u/k = 145.3$  K) was detected in G16.86–2.16. The results suggest that hot gas exists in G12.89+0.49 and G16.86–2.16, which is supported by the detection of the metastable inversion transition  $\text{NH}_3$  lines with the very-high-excitation energies,  $(J, K) = (8, 8)$  at 26.51898 GHz ( $E_u/k = 686$  K) and  $(J, K) = (9, 9)$  at 27.47794 GHz ( $E_u/k = 852$  K), with the GBT (Taniguchi et al. 2017b).

In G12.89+0.49 and G16.86–2.16, the line profiles of  $\text{CH}_3\text{OH}$  show wing emission suggestive of molecular outflow origins. In addition, the line widths (FWHM) of  $\text{CH}_3\text{OH}$  in these two sources ( $\sim 5 - 6$  km s<sup>-1</sup>) are larger than those in G28.28–0.36 ( $\sim 2 - 3$  km s<sup>-1</sup>). This may suggest that  $\text{CH}_3\text{OH}$  in G28.28–0.36 exists in less turbulent regions, as it is discussed in more detail in Section 5.6.

## 4. ANALYSES

<sup>1</sup> The  $V_{\text{LSR}}$  values of molecular emission lines are shifted by  $\sim 0.2$  km s<sup>-1</sup> due to bug in ASTE Newstar. Results and discussions in this paper are not affected by this bug.



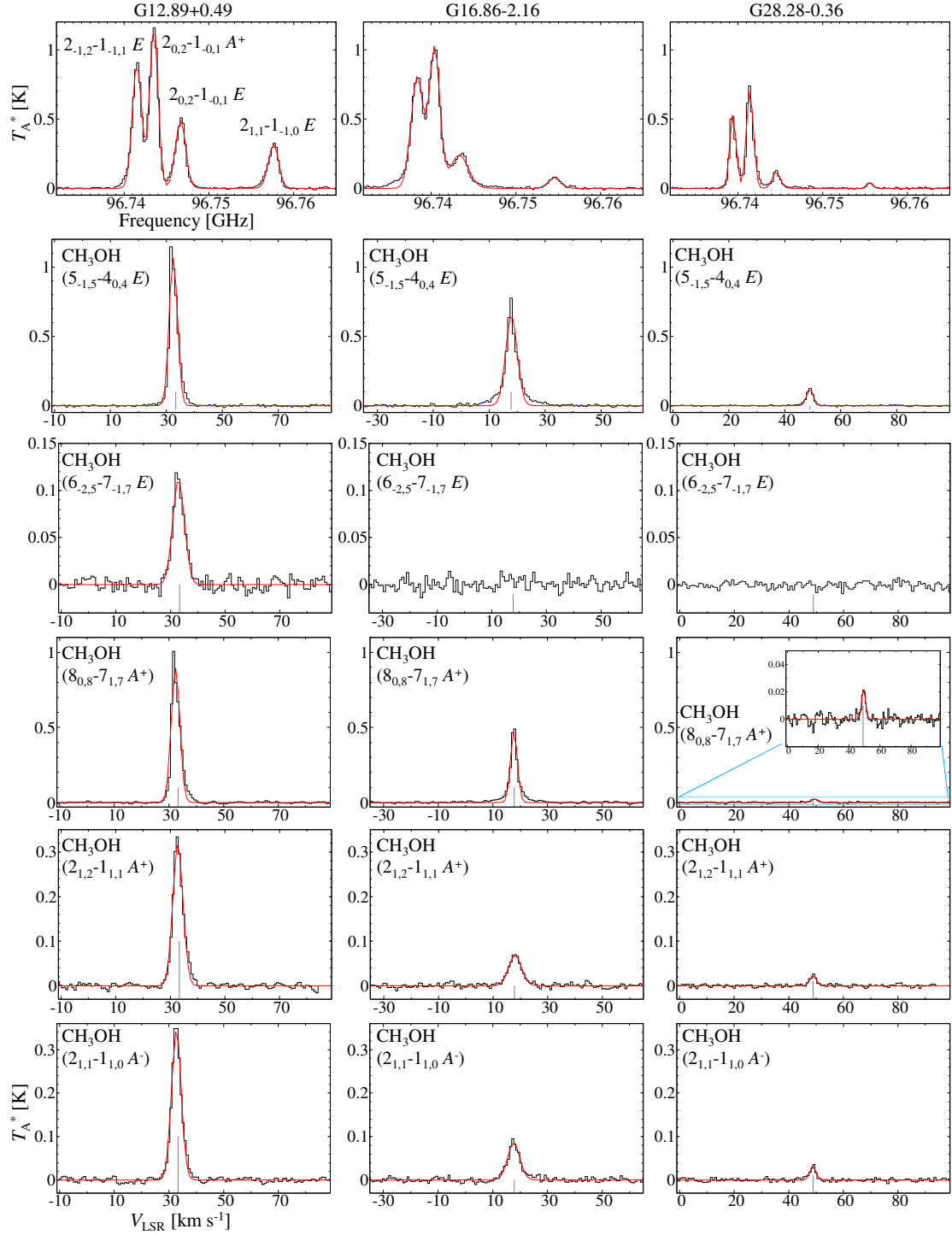


**Figure 3.** Spectra of  $\text{CH}_3\text{OH}$  in the three sources. The red lines show the Gaussian fitting results and gray vertical lines show the systemic velocity for each source.

**Table 5.** Spectral line parameters of CH<sub>3</sub>OH in the three sources with the Nobeyama 45-m telescope

Transition	Frequency <sup>a</sup> (GHz)	$E_u/k$ (K)	G12.89+0.49				G16.86−2.16				G28.28−0.36			
			$T_{\text{mb}}$ (K)	FWHM (km s <sup>−1</sup> )	$\int T_{\text{mb}} dv$ (K km s <sup>−1</sup> )	$V_{\text{LSR}}^b$ (km s <sup>−1</sup> )	$T_{\text{mb}}$ (K)	FWHM (km s <sup>−1</sup> )	$\int T_{\text{mb}} dv$ (K km s <sup>−1</sup> )	$V_{\text{LSR}}^b$ (km s <sup>−1</sup> )	$T_{\text{mb}}$ (K)	FWHM (km s <sup>−1</sup> )	$\int T_{\text{mb}} dv$ (K km s <sup>−1</sup> )	$V_{\text{LSR}}^b$ (km s <sup>−1</sup> )
			$5_{-1,5} - 4_{0,4} E$	84.521169	40.4	1.97 (8)	3.44 (14)	7.2 (4)	32.5	1.20 (6)	4.9 (2)	6.2 (4)	17.9	0.222 (8)
$6_{-2,5} - 7_{-1,7} E$	85.568084	74.7	0.206 (7)	5.06 (17)	1.11 (5)	32.9	< 0.018	...	...	...	< 0.011	...	...	...
$8_{0,8} - 7_{1,7} A^+$	95.169463	83.5	1.82 (7)	3.70 (15)	7.2 (4)	32.4	0.96 (4)	2.92 (13)	2.99 (18)	17.7	0.045 (4)	3.0 (3)	0.14 (2)	49.3
$2_{1,2} - 1_{1,1} A^+$	95.914309	21.4	0.664 (13)	4.39 (10)	3.10 (9)	32.7	0.141 (4)	5.55 (19)	0.83 (4)	18.0	0.050 (4)	2.8 (3)	0.149 (19)	48.9
$2_{-1,2} - 1_{-1,1} E$	96.739362	12.5	1.81 (2)	4.09 (6)	7.87 (15)	–	1.63 (2)	5.31 (9)	9.2 (2)	–	1.06 (3)	2.80 (10)	3.16 (14)	–
$2_{0,2} - 1_{0,1} A^+$	96.741375	7.0	2.39 (2)	3.60 (4)	9.14 (14)	–	2.05 (2)	4.50 (7)	9.81 (19)	–	1.42 (3)	3.02 (7)	4.57 (15)	–
$2_{0,2} - 1_{0,1} E$	96.744550	20.1	0.99 (2)	4.40 (11)	4.66 (15)	–	0.485 (18)	7.8 (4)	4.0 (2)	–	0.23 (3)	3.5 (5)	0.87 (16)	–
$2_{1,1} - 1_{1,0} E$	96.755511	28.0	0.64 (2)	4.47 (17)	3.06 (15)	–	0.16 (2)	5.2 (8)	0.87 (18)	–	0.08 (3)	2.6 (12)	0.22 (14)	–
$2_{1,1} - 1_{1,0} A^-$	97.582804	21.6	0.702 (12)	4.18 (8)	3.12 (8)	32.7	0.172 (7)	5.3 (2)	0.97 (6)	17.6	0.065 (6)	2.7 (3)	0.18 (2)	48.8

NOTE—Numbers in the parentheses are the standard deviation of the Gaussian fit, expressed in units of the last significant digits. The upper limits correspond to the  $3\sigma$  limits.

<sup>a</sup> Taken from the Cologne Database for Molecular Spectroscopy (CDMS; Müller et al. 2005).

<sup>b</sup> The errors are 0.85 km s<sup>−1</sup>, which corresponds to the velocity resolution (Section 2.1).

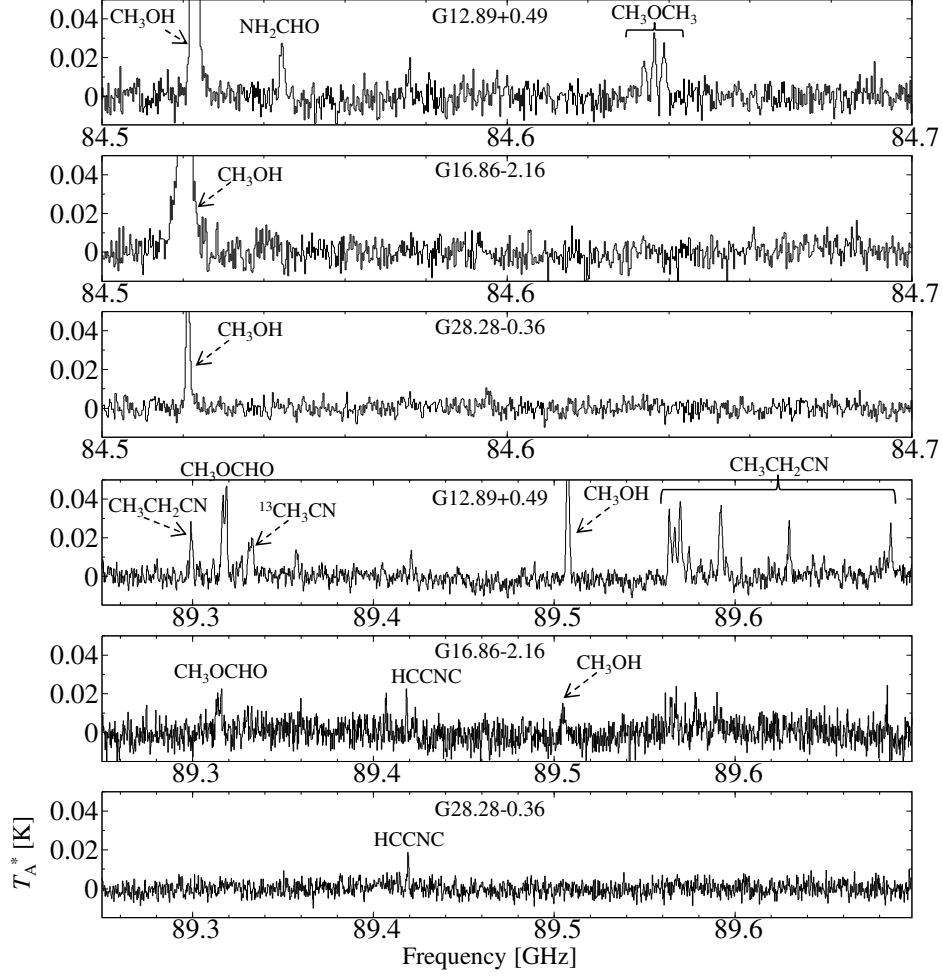


**Figure 4.** Spectra of the complex organic molecules in the 84.5–84.7 and 89.3–89.7 GHz bands in the three sources obtained with the Nobeyama 45-m telescope.

**Table 6.** Summary of detection of complex organic molecules in the three sources with the Nobeyama 45-m telescope

Species	G12.89+0.49	G16.86–2.16	G28.28–0.36
CH <sub>3</sub> OCHO	Y	Y	N
CH <sub>3</sub> CH <sub>2</sub> OH	Y	N	N
CH <sub>3</sub> CHO	Y	Y	Y
CH <sub>3</sub> OCH <sub>3</sub>	Y	N	N
NH <sub>2</sub> CHO	Y	N	N
CH <sub>2</sub> CHCN	Y	N	N
CH <sub>3</sub> CH <sub>2</sub> CN	Y	N	N

NOTE—‘Y’ and ‘N’ represent detection and non-detection with a S/N ratio above 4, respectively.

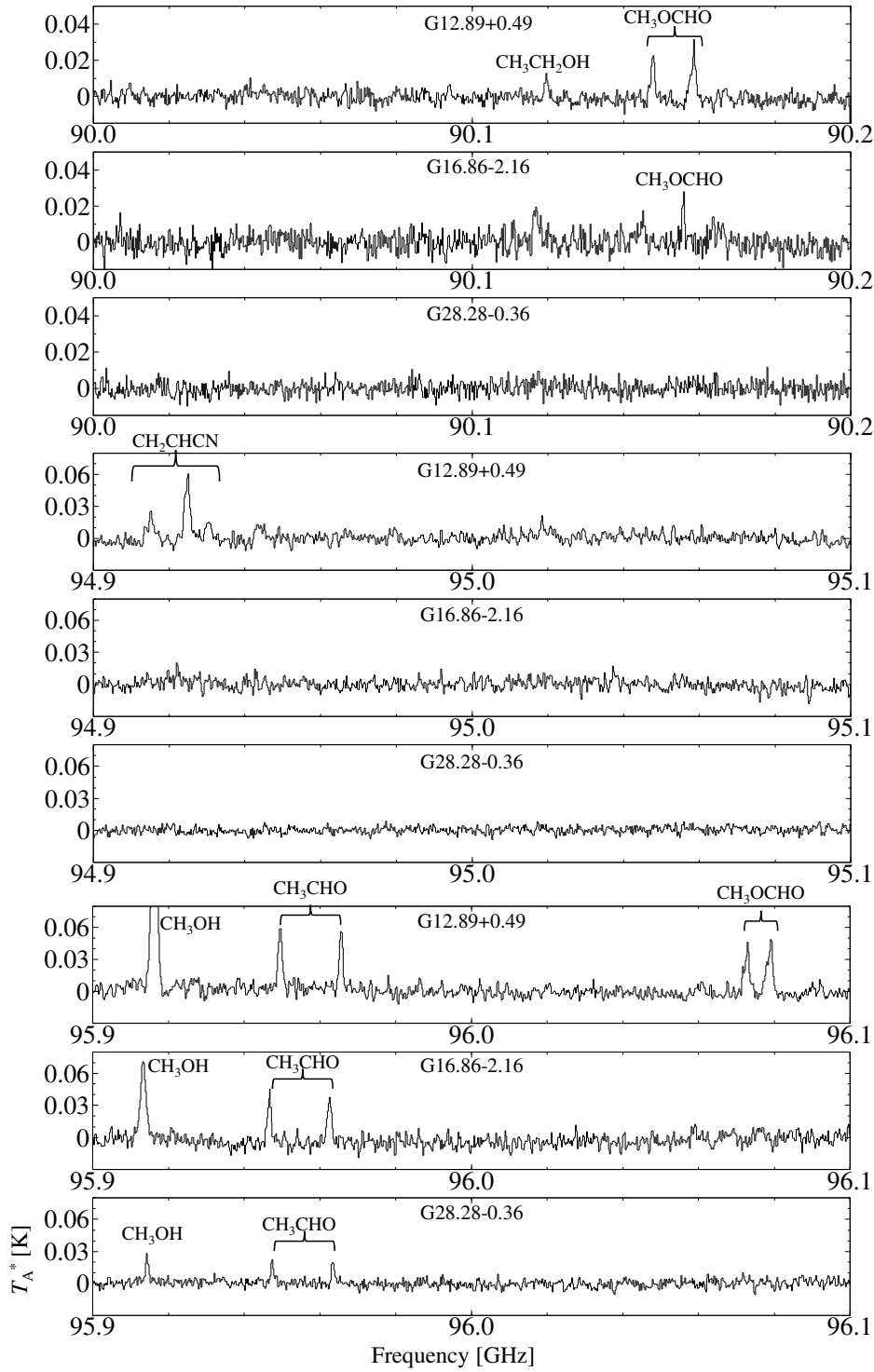


**Figure 5.** Spectra of the complex organic molecules in the 90.0–90.2, 94.9–95.1, and 95.9–96.1 GHz bands in the three sources obtained with the Nobeyama 45-m telescope.

**Table 7.** Spectral line parameters in the three sources with the ASTE 10-m telescope

Species & Transition	Frequency <sup>a</sup> (GHz)	$E_u/k$ (K)	G12.89+0.49				G16.86−2.16				G28.28−0.36			
			$T_{\text{mb}}$ (K)	FWHM (km s <sup>−1</sup> )	$\int T_{\text{mb}} dv^b$ (K km s <sup>−1</sup> )	$V_{\text{LSR}}^c$ (km s <sup>−1</sup> )	$T_{\text{mb}}$ (K)	FWHM (km s <sup>−1</sup> )	$\int T_{\text{mb}} dv^b$ (K km s <sup>−1</sup> )	$V_{\text{LSR}}^c$ (km s <sup>−1</sup> )	$T_{\text{mb}}$ (K)	FWHM (km s <sup>−1</sup> )	$\int T_{\text{mb}} dv^b$ (K km s <sup>−1</sup> )	$V_{\text{LSR}}^c$ (km s <sup>−1</sup> )
SO <sub>2</sub>														
18 <sub>4,14</sub> − 18 <sub>3,15</sub>	338.305993	196.8	0.13 (4) <sup>d</sup>	5.9 (9)	0.81 (9)	33.1	< 0.09	...	...	...	< 0.09	...	...	
CH <sub>3</sub> OH														
7 <sub>−1,7</sub> − 6 <sub>−1,6</sub> <i>E</i>	338.344628	70.5	1.23 (4)	4.6 (9)	5.99 (10)	32.9	0.82 (3)	4.5 (9)	3.94 (8)	17.3	0.17 (3)	2.2 (8)	0.40 (6)	48
7 <sub>0,7</sub> − 6 <sub>0,6</sub> <i>A</i> <sup>+</sup>	338.408681	65.0	1.50 (4)	5.1 (9)	8.06 (11)	33.0	1.07 (3)	4.8 (9)	5.42 (7)	17.2	0.19 (3)	2.5 (8)	0.49 (5)	49
7 <sub>−6,1</sub> − 6 <sub>−6,0</sub> <i>E</i>	338.430933	253.9	0.23 (4)	5.8 (9)	1.40 (9)	32.9	< 0.09	...	...	...	< 0.09	...	...	
7 <sub>6,1</sub> − 6 <sub>6,0</sub> <i>A</i> <sup>+</sup>	338.442344	258.7	0.26 (4)	4.5 (9)	1.22 (9)	33.0	< 0.09	...	...	...	< 0.09	...	...	
7 <sub>−5,2</sub> − 6 <sub>−5,1</sub> <i>E</i>	338.456499	189.0	0.26 (4)	5.0 (9)	1.38 (11)	32.9	< 0.09	...	...	...	< 0.09	...	...	
7 <sub>5,3</sub> − 6 <sub>5,2</sub> <i>E</i>	338.475290	201.1	0.25 (4)	5.2 (9)	1.42 (11)	32.7	< 0.09	...	...	...	< 0.09	...	...	
7 <sub>5,3</sub> − 6 <sub>5,2</sub> <i>A</i> <sup>+</sup>	338.486337	202.9	0.25 (4)	5.9 (9)	1.55 (11)	33.2	< 0.09	...	...	...	< 0.09	...	...	
7 <sub>−4,4</sub> − 6 <sub>−4,3</sub> <i>E</i>	338.504099	152.9	0.30 (4)	6.0 (9)	1.91 (10)	32.8	< 0.09	...	...	...	< 0.09	...	...	
7 <sub>4,3</sub> − 6 <sub>4,2</sub> <i>A</i> <sup>+</sup>	338.512627	145.3	0.51 (4)	4.7 (9)	2.56 (11)	32.7	0.14 (3)	6.1 (9)	0.92 (10)	17.7	< 0.09	...	...	
7 <sub>4,3</sub> − 6 <sub>4,2</sub> <i>E</i>	338.530249	161.0	0.27 (4)	6.0 (9)	1.72 (9)	32.8	< 0.09	...	...	...	< 0.09	...	...	
7 <sub>3,5</sub> − 6 <sub>3,4</sub> <i>A</i> <sup>+</sup>	338.540795	114.8	0.56 (4)	6.1 (9)	3.64 (12)	32.0	0.15 (3)	6.7 (9)	1.10 (10)	16.1	< 0.09	...	...	
7 <sub>−3,5</sub> − 6 <sub>−3,4</sub> <i>E</i>	338.559928	127.7	0.36 (4)	4.5 (9)	1.73 (10)	32.8	< 0.09	...	...	...	< 0.09	...	...	
7 <sub>3,4</sub> − 6 <sub>3,3</sub> <i>E</i>	338.583195	112.7	0.36 (4)	5.2 (9)	2.00 (10)	33.0	< 0.09	...	...	...	< 0.09	...	...	
7 <sub>1,6</sub> − 6 <sub>1,5</sub> <i>E</i>	338.614999	86.1	0.73 (4)	5.5 (9)	4.28 (11)	33.3	0.26 (3)	4.3 (9)	1.20 (8)	17.3	< 0.09	...	...	
7 <sub>2,5</sub> − 6 <sub>2,4</sub> <i>A</i> <sup>+</sup>	338.639939	102.7	0.45 (4)	4.9 (9)	2.36 (11)	33.2	0.12 (3)	5.8 (9)	0.72 (9)	17.9	< 0.09	...	...	
7 <sub>−2,6</sub> − 6 <sub>−2,5</sub> <i>E</i>	338.72294	90.9	0.89 (4)	4.9 (9)	4.64 (11)	32.3	0.51 (3)	5.8 (9)	3.10 (7)	18.2	< 0.09	...	...	
14 <sub>1,13</sub> − 14 <sub>0,14</sub> <i>A</i> <sup>−+</sup>	349.10702	260.2	0.36 (4)	6.0 (9)	2.29 (12)	33.2	< 0.09	...	...	...	< 0.09	...	...	
<sup>13</sup> CH <sub>3</sub> OH														
13 <sub>0,13</sub> − 12 <sub>1,12</sub> <i>A</i> <sup>+</sup>	338.759948	205.9	0.17 (4)	4.5 (9)	0.80 (6)	33.0	< 0.09	...	...	...	< 0.09	...	...	
H <sub>2</sub> CS														
10 <sub>1,9</sub> − 9 <sub>1,8</sub>	348.5343647	105.2	0.55 (4)	4.5 (9)	2.64 (11)	32.9	0.10 (3)	6.2 (9)	0.64 (6)	17.4	< 0.09	...	...	
CCH														
$N = 4 - 3, J = 9/2 - 7/2$	349.3374558	41.9	1.17 (4)	4.2 (9)	5.22 (11)	33.7	1.12 (3)	3.2 (9)	3.82 (8)	16.8	0.34 (3)	3.4 (9)	1.25 (7)	48
$N = 4 - 3, J = 7/2 - 5/2$	349.3992738	41.9	0.80 (4) <sup>e</sup>	3.8 (9)	3.27 (11)	32.1	0.86 (3)	3.3 (9)	3.04 (8)	17.1	0.25 (3)	3.4 (9)	0.92 (7)	48
CH <sub>3</sub> CN														
$J_K = 19_6 - 18_6$	349.2123106	424.7	0.14 (4)	5.4 (9)	0.81 (12)	33.1	< 0.09	...	...	...	< 0.09	...	...	
$J_K = 19_5 - 18_5$	349.2860057	346.2	0.16 (4)	5.8 (9)	0.98 (12)	33.9	< 0.09	...	...	...	< 0.09	...	...	
$J_K = 19_4 - 18_4$	349.3463428	282.0	0.20 (4) <sup>e</sup>	5.1 (9)	1.07 (11)	33.3	< 0.09	...	...	...	< 0.09	...	...	
$J_K = 19_2 - 18_2$	349.4268497	196.3	0.23 (4)	5.3 (9)	1.32 (11)	33.0	< 0.09	...	...	...	< 0.09	...	...	

NOTE—Numbers in the parentheses are the standard deviation, expressed in units of the last significant digits. The upper limits correspond to the  $3\sigma$  limits.

<sup>a</sup> Taken from the Cologne Database for Molecular Spectroscopy (CDMS; Müller et al. 2005).

<sup>b</sup> The errors were derived using the following formula;  $\Delta T_{\text{mb}} \sqrt{n} \Delta v$ , where  $\Delta T_{\text{mb}}$ ,  $n$ ,  $\Delta v$  are the rms noise in the emission-free regions, the number of channels, and velocity resolution per channel, respectively.

<sup>c</sup> The errors are 0.86 km s<sup>−1</sup>, which corresponds to the velocity resolution (Section 2.2).

<sup>d</sup> Tentative detection with the signal-to-noise ratio above 3.

<sup>e</sup> These lines are contaminated and fitting results are tentative.

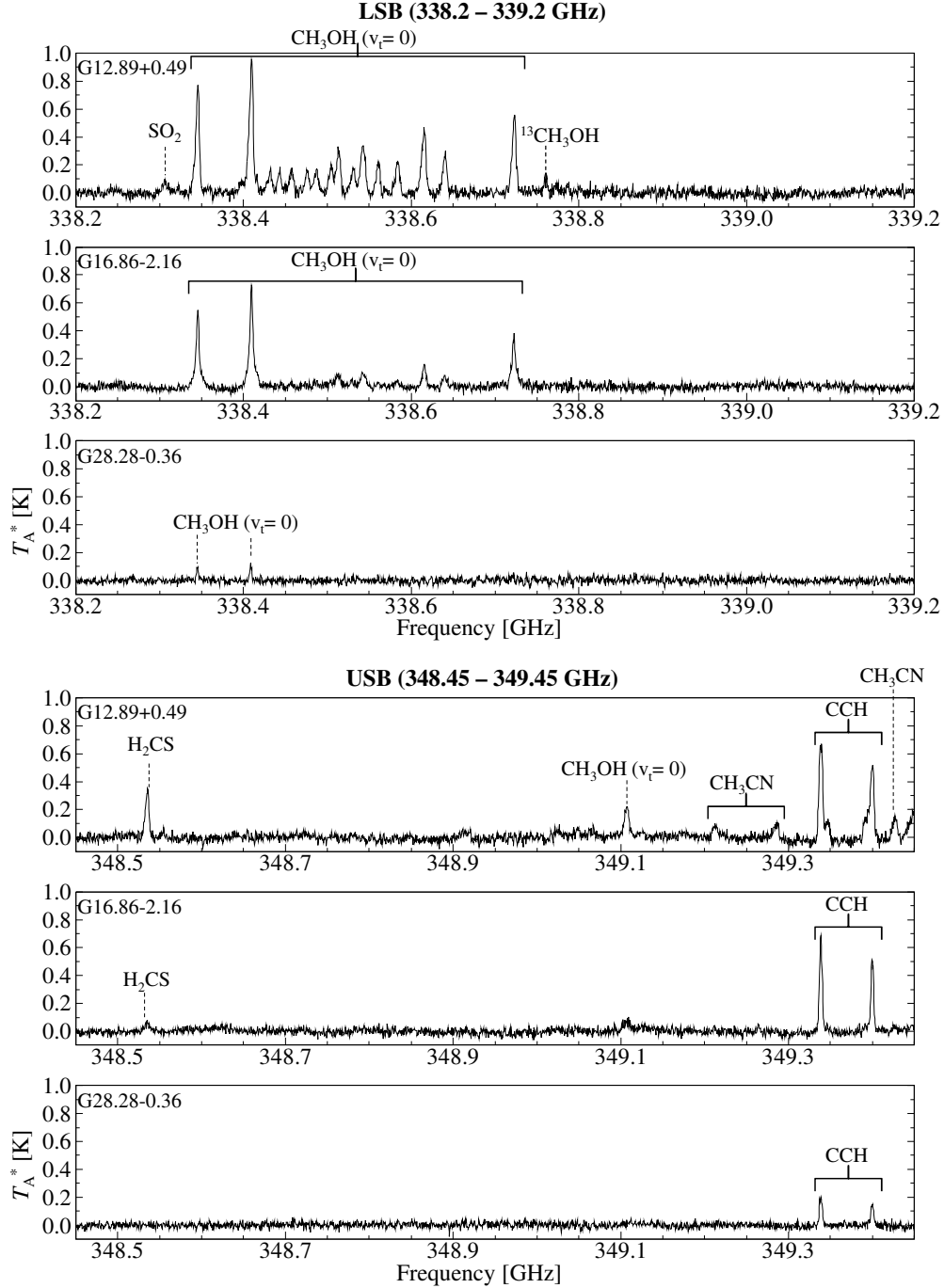


**Figure 6.** Spectra in the 338.2–339.2 and 348.45–349.45 GHz bands toward the three sources with the ASTE 10-m telescope.

#### 4.1. Rotational Diagram Analysis

We derived the rotational temperatures and beam-averaged column densities of  $\text{HC}_3\text{N}$ ,  $\text{CH}_3\text{CCH}$ , and  $\text{CH}_3\text{OH}$  with the beam size of  $18''$  in the three sources from the rotational diagram analysis, using the following formula (Goldsmith & Langer 1999);

$$\ln \frac{3k \int T_{\text{mb}} dv}{8\pi^3 \nu S \mu^2} = \ln \frac{N}{Q(T_{\text{rot}})} - \frac{E_{\text{u}}}{kT_{\text{rot}}}, \quad (1)$$

where  $k$  is the Boltzmann constant,  $S$  is the line strength,  $\mu$  is the permanent electric dipole moment,  $N$  is the column density, and  $Q(T_{\text{rot}})$  is the partition function. The permanent electric dipole moments are 3.7312, 0.784, and 0.899 D for  $\text{HC}_3\text{N}$ ,  $\text{CH}_3\text{CCH}$ , and  $\text{CH}_3\text{OH}$ , respectively. We used  $\int T_{\text{mb}} dv$  values summarized in Tables 3, 4, and 5.

Figure 7 shows the fitting results of  $\text{HC}_3\text{N}$ ,  $\text{CH}_3\text{CCH}$ , and  $\text{CH}_3\text{OH}$  in the three sources. The errors include the Gaussian fitting errors, the uncertainties from the main beam efficiency of 10%, the chopper-wheel method of 10%, and pointing calibration error of 30%. The derived rotational temperatures and column densities are summarized in Table 8.

In the case of  $\text{HC}_3\text{N}$ , we added data of the  $J = 3 - 2$  transition obtained with the GBT (Table 3 in Taniguchi et al. 2017b). The beam sizes are different among the three transitions,  $27''$ ,  $37''$ , and  $18''$  for the  $J = 3 - 2$ ,  $5 - 4$ , and  $10 - 9$ , respectively. Assuming a small beam filling factor, we multiplied the integrated intensities of the GBT data by  $(\frac{27''}{18''})^2$  and the 45 GHz band data by  $(\frac{37''}{18''})^2$  for the correction of the different beam sizes (filled circles in Figure 7). The red lines are the best fitting results for  $J = 5 - 4$  without beam size correction and  $J = 10 - 9$  transitions, and the green lines show the fitting results for the three transitions with beam size correction. In the case of the fitting for the  $J = 5 - 4$  and  $10 - 9$  transitions, the  $1\sigma$  fluctuation in the integrated intensity causes unlikely large errors in the derived rotational temperature and column density (e.g.,  $T_{\text{rot}} \sim 600$  K), and we do not include the errors in Table 8. All of the three transitions are better fitted with beam size correction. The fitting results imply that the spatial distribution of  $\text{HC}_3\text{N}$  is smaller than  $18''$ , corresponding to  $\sim 0.07 - 0.1$  pc radii at the source distances (Table 2), like in the case for  $\text{HC}_5\text{N}$  (Taniguchi et al. 2017b). Taniguchi et al. (2017b) derived the rotational temperatures of  $\text{HC}_5\text{N}$  with beam size correction to be  $\sim 13 - 20$  K in the three sources. The different rotational temperatures between  $\text{HC}_3\text{N}$  and  $\text{HC}_5\text{N}$  probably arise from the fact that we observed only lower excitation-energy lines ( $E_{\text{u}}/k < 24.0$  K), compared to  $\text{HC}_5\text{N}$  ( $E_{\text{u}}/k \leq 100$  K; Taniguchi et al. 2017b), and the presence of complex excitation conditions.

In the case of  $\text{CH}_3\text{CCH}$ , we multiplied the integrated intensities of the  $J = 6 - 5$  transition lines by  $(\frac{85.4\text{GHz}}{102.5\text{GHz}})^2$  in order to correct the values for the  $18''$  beam size at the 85 GHz band in G12.89+0.49 and G16.86-2.16, because data of the  $J = 6 - 5$  transition are systematically higher than those of the  $J = 5 - 4$  transition. In Figure 7, open and filled circles represent the integrated intensities without and with correction of frequency dependence of the beam size, respectively. The black lines show the fitting results with correction of frequency dependence. All of the data can be fitted simultaneously, which means that the spatial distribution of  $\text{CH}_3\text{CCH}$  is smaller than  $18''$ . This is the same case as for  $\text{HC}_3\text{N}$  and  $\text{HC}_5\text{N}$ . The derived rotational temperatures are  $33_{-9}^{+20}$ ,  $29_{-8}^{+15}$ , and  $23_{-6}^{+9}$  K in G12.89+0.40, G16.86-2.16, and G28.28-0.36, respectively.

In the case of  $\text{CH}_3\text{OH}$ , we fitted the data using all the lines in the 85-98 GHz band summarized in Table 5, and the fitting results are shown by the black lines in Figure 7. As is the case of  $\text{CH}_3\text{CCH}$ , we derived beam-averaged column densities a beam size of  $18''$ , correcting the frequency dependence of the beam size by multiplying the integrated intensities of the lines in the 95-98 GHz by  $(\frac{85\text{GHz}}{\nu\text{GHz}})^2$ , where  $\nu$  is the frequency of each line. The rotational temperatures are  $42_{-13}^{+33}$ ,  $36_{-9}^{+18}$ , and  $18_{-3}^{+5}$  K in G12.89+0.49, G16.86-2.16, and G28.28-0.36, respectively (Table 8). Purcell et al. (2009) derived the rotational temperatures of  $\text{CH}_3\text{OH}$  to be  $5 \pm 0.8$ ,  $6 \pm 0.1$ , and  $5 \pm 0.5$  K in G12.89+0.49, G16.86-2.16, and G28.28-0.36, respectively, from fitting only three or four line transitions, which was interpreted as  $\text{CH}_3\text{OH}$  being sub-thermally excited. This does not seem to be the case when considering more  $\text{CH}_3\text{OH}$  transitions in the derivation of the rotational temperature.

#### 4.2. Column Densities of the D and $^{13}\text{C}$ Isotopologues of $\text{HC}_3\text{N}$

We derived the column densities of the D and  $^{13}\text{C}$  isotopologues of  $\text{HC}_3\text{N}$  in the three sources assuming the LTE condition (Goldsmith & Langer 1999). We used the following formulae;

$$\tau = -\ln \left[ 1 - \frac{T_{\text{mb}}}{J(T_{\text{ex}}) - J(T_{\text{bg}})} \right] \quad (2)$$

where

$$J(T) = \frac{h\nu}{k} \left\{ \exp\left(\frac{h\nu}{kT}\right) - 1 \right\}^{-1}, \quad (3)$$

and

$$N = \tau \frac{3h\Delta\nu}{8\pi^3} \sqrt{\frac{\pi}{4\ln 2}} Q \frac{1}{\mu^2} \frac{1}{J_{\text{lower}} + 1} \exp\left(\frac{E_{\text{lower}}}{kT_{\text{ex}}}\right) \left\{ 1 - \exp\left(-\frac{h\nu}{kT_{\text{ex}}}\right) \right\}^{-1}. \quad (4)$$

In Equation (2),  $\tau$  denotes the optical depth, and  $T_{\text{mb}}$  the peak intensities summarized in Table 3.  $T_{\text{ex}}$  and  $T_{\text{bg}}$  are the excitation temperature and the cosmic microwave background temperature ( $\simeq 2.73$  K). We used the rotational



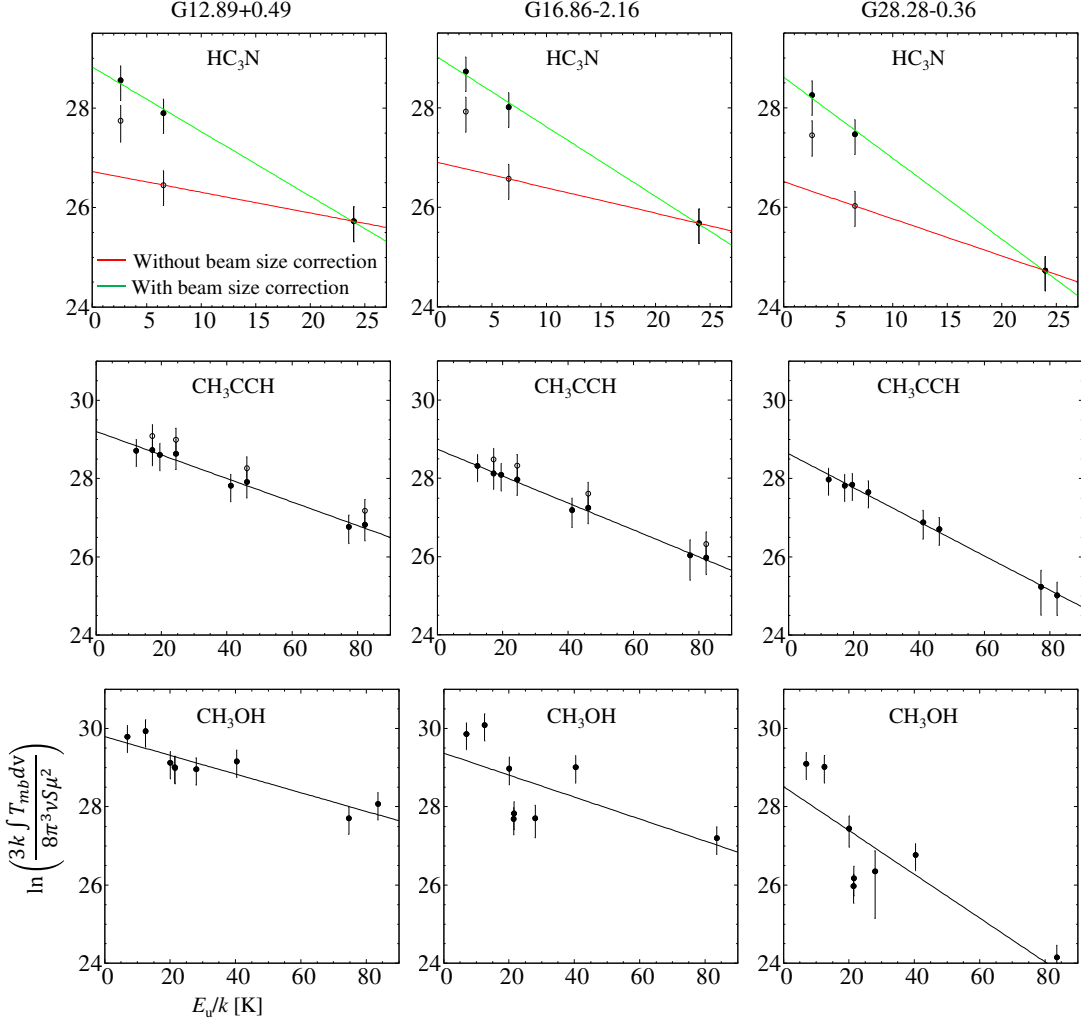


**Figure 7.** Rotational diagram of  $\text{HC}_3\text{N}$ ,  $\text{CH}_3\text{CCH}$ , and  $\text{CH}_3\text{OH}$  in the three sources.  $\text{HC}_3\text{N}$  (upper panels): The filled and open circles represent with and without beam size correction, respectively. The red line is the fitting results for the  $J = 5 - 4$  data without beam size correction and  $J = 10 - 9$  data. The green line shows the fitting results for all of the lines with the beam size correction.  $\text{CH}_3\text{CCH}$  (middle panels): The filled and open circles represent with and without correction of frequency dependence, respectively. The black lines show the fitting results with correction of frequency dependence.  $\text{CH}_3\text{OH}$  (lower panels): The black lines show the fitting results for all of the observed lines.

temperatures of  $\text{HC}_3\text{N}$  summarized in Table 8 as the excitation temperatures. We calculated two cases of excitation temperatures (Table 8) for each source.  $J(T)$  in Equation (3) is the effective temperature equivalent to that in the Rayleigh-Jeans law. In Equation (4),  $N$  is the column density,  $\Delta v$  is the line width (FWHM, Table 3),  $Q$  is the partition function,  $\mu$  is the permanent electric dipole moment, and  $E_{\text{lower}}$  is the energy of the lower rotational energy level. The electric dipole moments are 3.7408 D and 3.73172 D for  $\text{DC}_3\text{N}$  and the three  $^{13}\text{C}$  isotopologues, respectively. The derived column densities and the D/H and  $^{12}\text{C}/^{13}\text{C}$  ratios are summarized in Table 9.

## 5. DISCUSSION

In this section, we will discuss comparisons of the chemical composition among MYSOs using  $\text{CH}_3\text{OH}$ ,  $\text{CH}_3\text{CCH}$ , and  $\text{HC}_3\text{N}$ , all of which are considered to be in the lukewarm envelopes (Table 8). In the following discussion, we assume that the spatial distributions of  $\text{CH}_3\text{OH}$ ,  $\text{CH}_3\text{CCH}$ , and  $\text{HC}_3\text{N}$  are similar to each other. This assumption is based on the following results; the source sizes of both  $\text{HC}_3\text{N}$  and  $\text{CH}_3\text{CCH}$  seem to be smaller than  $18''$  (see Taniguchi et al. (2017b) and Section 4.1), and the rotational temperatures of  $\text{CH}_3\text{OH}$  are comparable with those of  $\text{CH}_3\text{CCH}$  in our

**Table 8.** The rotational temperatures and beam-averaged column densities of HC<sub>3</sub>N, CH<sub>3</sub>CCH, and CH<sub>3</sub>OH

Species	G12.89+0.49		G16.86−2.16		G28.28−0.36	
	$T_{\text{rot}}$	$N$	$T_{\text{rot}}$	$N$	$T_{\text{rot}}$	$N$
	(K)	(cm <sup>−2</sup> )	(K)	(cm <sup>−2</sup> )	(K)	(cm <sup>−2</sup> )
HC <sub>3</sub> N						
$J = 5 - 4$ & $10 - 9$	24	$4.4 \times 10^{13}$	20	$4.3 \times 10^{13}$	13.4	$2.0 \times 10^{13}$
All	$7.7^{+1.6}_{-2.8}$	$(1.4 \pm 0.3) \times 10^{14}$	$7.2^{+1.4}_{-2.4}$	$(1.3 \pm 0.3) \times 10^{14}$	$6.2^{+1.1}_{-1.7}$	$(7.6 \pm 2.1) \times 10^{13}$
CH <sub>3</sub> CCH	$33^{+20}_{-9}$	$1.0^{+0.11}_{-0.02} \times 10^{15}$	$29^{+15}_{-8}$	$5.4^{+0.7}_{-0.8} \times 10^{14}$	$23^{+9}_{-6}$	$3.7^{+0.5}_{-0.9} \times 10^{14}$
CH <sub>3</sub> OH	$42^{+33}_{-13}$	$2.9^{+1.9}_{-1.3} \times 10^{15}$	$36^{+18}_{-9}$	$1.5^{+0.9}_{-0.7} \times 10^{15}$	$18^{+5}_{-3}$	$2.3^{+1.6}_{-1.1} \times 10^{14}$

NOTE—The errors represent the standard deviation.

**Table 9.** The column densities of the D and <sup>13</sup>C isotopologues of HC<sub>3</sub>N

Species	G12.89+0.49		G16.86−2.16		G28.28−0.36	
	$N$	D/H,	$N$	D/H,	$N$	D/H,
	(cm <sup>−2</sup> )	<sup>12</sup> C/ <sup>13</sup> C	(cm <sup>−2</sup> )	<sup>12</sup> C/ <sup>13</sup> C	(cm <sup>−2</sup> )	<sup>12</sup> C/ <sup>13</sup> C
	$T_{\text{ex}} = 24$ K (fixed)		$T_{\text{ex}} = 20$ K (fixed)		$T_{\text{ex}} = 13.4$ K (fixed)	
DC <sub>3</sub> N	$< 6.2 \times 10^{10}$	$< 0.0014$	$(5.5 \pm 1.5) \times 10^{11}$	$0.013 \pm 0.003$	$(3.7 \pm 1.0) \times 10^{11}$	$0.018 \pm 0.005$
H <sup>13</sup> CCCN	$(5.8 \pm 1.7) \times 10^{11}$	$76 \pm 23$	$< 2.6 \times 10^{11}$	$< 165$	$(6.8 \pm 1.8) \times 10^{11}$	$30 \pm 8$
HC <sup>13</sup> CCN	$< 1.9 \times 10^{11}$	$< 237$	$(7.6 \pm 2.8) \times 10^{11}$	$57 \pm 21$	$(1.0 \pm 0.3) \times 10^{12}$	$20 \pm 5$
HCC <sup>13</sup> CN	$(7.1 \pm 1.9) \times 10^{11}$	$63 \pm 16$	$(1.8 \pm 0.4) \times 10^{12}$	$24 \pm 5$	$(8.2 \pm 2.3) \times 10^{11}$	$25 \pm 7$
	$T_{\text{ex}} = 7.7$ K (fixed)		$T_{\text{ex}} = 7.2$ K (fixed)		$T_{\text{ex}} = 6.2$ K (fixed)	
DC <sub>3</sub> N	$< 5.4 \times 10^{11}$	$< 0.0046$	$(4.9 \pm 1.4) \times 10^{12}$	$0.037 \pm 0.010$	$(3.3 \pm 0.9) \times 10^{12}$	$0.043 \pm 0.012$
H <sup>13</sup> CCCN	$(2.5 \pm 0.8) \times 10^{12}$	$46 \pm 14$	$< 1.2 \times 10^{12}$	$< 114$	$(3.1 \pm 0.8) \times 10^{12}$	$24 \pm 7$
HC <sup>13</sup> CCN	$< 8.2 \times 10^{11}$	$< 142$	$(3.4 \pm 1.3) \times 10^{12}$	$38 \pm 14$	$(4.7 \pm 1.2) \times 10^{12}$	$16 \pm 4$
HCC <sup>13</sup> CN	$(3.1 \pm 0.8) \times 10^{12}$	$37 \pm 10$	$(6.0 \pm 1.4) \times 10^{12}$	$22 \pm 5$	$(3.9 \pm 1.1) \times 10^{12}$	$19 \pm 5$

 NOTE—The errors represent the standard deviation. The upper limits were derived using the 1 $\sigma$  noise level.

three sources. Nitrogen-bearing COMs are usually originated from hot cores (e.g., Bisschop et al. 2007), and thus we do not include them in discussion. We will also discuss the relationship between the line width and excitation energy of rotational lines of CH<sub>3</sub>OH.

### 5.1. Comparisons of Fractional Abundances in the High-Mass Star-Forming Regions

We derived the fractional abundances of HC<sub>3</sub>N, CH<sub>3</sub>OH, and CH<sub>3</sub>CCH,  $X(a) = N(a)/N(\text{H}_2)$ , in the three sources. The H<sub>2</sub> column densities,  $N(\text{H}_2)$ , in the three sources were derived by Taniguchi et al. (2017b). The  $N(\text{H}_2)$  values and the fractional abundances of HC<sub>3</sub>N, CH<sub>3</sub>OH, CH<sub>3</sub>CCH, and HC<sub>5</sub>N derived by Taniguchi et al. (2017b) are summarized in Table 10. The derived  $X(\text{CH}_3\text{OH})$  values are  $1.2^{+1.8}_{-0.9} \times 10^{-7}$ ,  $8.8^{+11}_{-5.8} \times 10^{-8}$ , and  $4.6^{+7.0}_{-3.4} \times 10^{-8}$  in G12.89+0.49, G16.86−2.16, and G28.28−0.36, respectively. The  $X(\text{CH}_3\text{CCH})$  values are derived to be  $4.2^{+2.8}_{-2.2} \times 10^{-8}$ ,  $3.2^{+1.9}_{-1.5} \times 10^{-8}$ , and  $7.6^{+5.2}_{-4.4} \times 10^{-8}$  in G12.89+0.49, G16.86−2.16, and G28.28−0.36, respectively. We derive the  $X(\text{HC}_3\text{N})$  values for two cases, fitting results of two transitions and all transitions (Table 8). Figure 8 shows their fractional abundances in the three sources. All of the column densities including the molecular hydrogen were derived as beam-averaged values for a beam size of 18". More accurate column densities and fractional abundances can be obtained in the future via interferometric observations that resolve the size of the sources.

**Table 10.** The  $N(\text{H}_2)$  and fractional abundances of  $\text{CH}_3\text{OH}$ ,  $\text{CH}_3\text{CCH}$ ,  $\text{HC}_3\text{N}$ , and  $\text{HC}_5\text{N}$  in the three sources

Source	$N(\text{H}_2)^a$ ( $\times 10^{22} \text{ cm}^{-2}$ )	$X(\text{CH}_3\text{OH})$ ( $\times 10^{-8}$ )	$X(\text{CH}_3\text{CCH})$ ( $\times 10^{-8}$ )	$X(\text{HC}_3\text{N})^b$ ( $\times 10^{-9}$ )	$X(\text{HC}_3\text{N})^c$ ( $\times 10^{-9}$ )	$X(\text{HC}_5\text{N})^a$ ( $\times 10^{-10}$ )
G12.89+0.49	$2.4^{+2.5}_{-0.8}$	$12^{+18}_{-9}$	$4.2^{+2.8}_{-2.2}$	$1.8 \pm 0.9$	$5.8^{+4.8}_{-3.6}$	$9.9^{+6.1}_{-5.4}$
G16.86−2.16	$1.7^{+1.0}_{-0.5}$	$8.8^{+11}_{-5.8}$	$3.2^{+1.9}_{-1.5}$	$2.5^{+1.1}_{-0.9}$	$7.7^{+5.7}_{-3.9}$	$16 \pm 7$
G28.28−0.36	$0.49^{+0.42}_{-0.16}$	$4.6^{+7.0}_{-3.4}$	$7.6^{+5.2}_{-4.4}$	$4.1^{+2.0}_{-1.9}$	$16^{+14}_{-9.5}$	$42^{+26}_{-20}$

NOTE—The errors represent the standard deviation. These values are averaged ones with the beam size of  $18''$ .

<sup>a</sup> Taniguchi et al. (2017b)

<sup>b</sup> The  $\text{HC}_3\text{N}$  column densities were derived from  $J = 5 - 4$  and  $10 - 9$ .

<sup>c</sup> The  $\text{HC}_3\text{N}$  column densities were derived from three rotational transitions.

Although our sample is small, there seems to be an anti-correlation between  $X(\text{CH}_3\text{OH})$  and  $X(\text{HC}_5\text{N})$ . G12.89+0.49 shows the highest  $X(\text{CH}_3\text{OH})$  value and the lowest  $X(\text{HC}_5\text{N})$  value among the three sources, while G28.28−0.36 shows the lowest  $X(\text{CH}_3\text{OH})$  value and the highest  $X(\text{HC}_5\text{N})$  value. We further discuss the relationship between  $\text{HC}_5\text{N}$  and  $\text{CH}_3\text{OH}$  in Section 5.2. The  $X(\text{HC}_3\text{N})$  has a positive correlation with  $X(\text{HC}_5\text{N})$ , while a negative correlation with  $X(\text{CH}_3\text{OH})$ .

The  $X(\text{CH}_3\text{CCH})$  values in the three sources are consistent within their  $1\sigma$  errors, and we cannot find any clear correlations between  $\text{HC}_5\text{N}$  and  $\text{CH}_3\text{CCH}$ . According to the gas-grain-bulk three-phase chemical network simulation (Majumdar et al. 2016, 2017a,b) results assuming that the temperatures are 20 and 30 K and the density is  $10^5 \text{ cm}^{-3}$ ,  $\text{CH}_3\text{CCH}$  is formed on the grains and desorbed non-thermally (Hasegawa & Herbst 1993; Garrod et al. 2007).  $\text{HC}_5\text{N}$  is formed in the gas phase mainly by the neutral-neutral reaction of  $\text{CN} + \text{C}_4\text{H}_2$  and the electron recombination reaction of  $\text{H}_2\text{C}_5\text{N}^+$ . The neutral-neutral reaction is also a main formation pathway to  $\text{HC}_5\text{N}$  in the model by Chapman et al. (2009). Chapman et al. (2009) suggested that  $\text{C}_4\text{H}_2$  is formed by the reaction of  $\text{C}_2\text{H}_2 + \text{CCH}$ .  $\text{C}_2\text{H}_2$  can be formed in the gas phase from  $\text{CH}_4$  (Hassel et al. 2008) and can be directly evaporated from grain mantles (Lahuis & van Dishoeck 2000). Hence, the productions of  $\text{CH}_3\text{CCH}$  and  $\text{HC}_5\text{N}$  seem to be related to the grain-surface reactions even in the lukewarm envelopes ( $T \sim 20 - 30 \text{ K}$ ). No correlation between  $\text{CH}_3\text{CCH}$  and  $\text{HC}_5\text{N}$  may imply that there is no direct relationship between them, which is also indicated in the chemical network simulation.

## 5.2. A Variety of the $N(\text{HC}_5\text{N})/N(\text{CH}_3\text{OH})$ Ratio

Taniguchi et al. (2017b) found that the  $N(\text{HC}_5\text{N})/W(\text{CH}_3\text{OH})$  ratio, where  $W$  represents the integrated intensity, varies by more than one order of magnitude among the three sources, and suggested the possibility of the chemical differentiation. In this paper, we derived the  $\text{CH}_3\text{OH}$  column densities in the three sources, and then we calculated the  $N(\text{HC}_5\text{N})/N(\text{CH}_3\text{OH})$  ratios in the observed three sources, as shown in Figure 9. We also added the data toward the high-mass protostellar object NGC2264 CMM3 (Watanabe et al. 2015). Watanabe et al. (2015) derived  $N(\text{HC}_5\text{N})$  and  $N(\text{CH}_3\text{OH})$  to be  $(2.5 \pm 0.9) \times 10^{13} \text{ cm}^{-2}$  and  $(1.8 \pm 0.2) \times 10^{15} \text{ cm}^{-2}$ , respectively. We took the cold component value for  $\text{CH}_3\text{OH}$ , because its rotational temperature ( $24.3 \pm 2.6 \text{ K}$ ) is comparable with that of  $\text{HC}_5\text{N}$  ( $25.8 \pm 4.6 \text{ K}$ ) in NGC2264 CMM3 (Watanabe et al. 2015).

The  $N(\text{HC}_5\text{N})/N(\text{CH}_3\text{OH})$  ratio in G28.28−0.36 ( $0.091^{+0.109}_{-0.039}$ ) is higher than that in G12.89+0.49 ( $0.008^{+0.008}_{-0.004}$ ) by one order of magnitude, and those in G16.86−2.16 ( $0.019^{+0.017}_{-0.008}$ ) and NGC2264 CMM3 ( $0.014^{+0.007}_{-0.006}$ ) by a factor of  $\sim 5$ .

As Taniguchi et al. (2017b) discussed, the  $\text{HC}_5\text{N}$  molecules can be formed from  $\text{CH}_4$  (WCCC, Aikawa et al. 2008; Hassel et al. 2008) and/or  $\text{C}_2\text{H}_2$  (Chapman et al. 2009), which could be evaporated from grain mantles.  $\text{CH}_3\text{OH}$  is mainly formed by the successive hydrogenation reaction of  $\text{CO}$  molecules on dust grains, while  $\text{CH}_4$ , may be  $\text{C}_2\text{H}_2$  (Lahuis & van Dishoeck 2000) as well, are formed by the hydrogenation reaction of  $\text{C}$  atoms on dust grains. Therefore, the chemical differentiation in the lukewarm envelope may reflect the different ice chemical composition among the MYSOs.

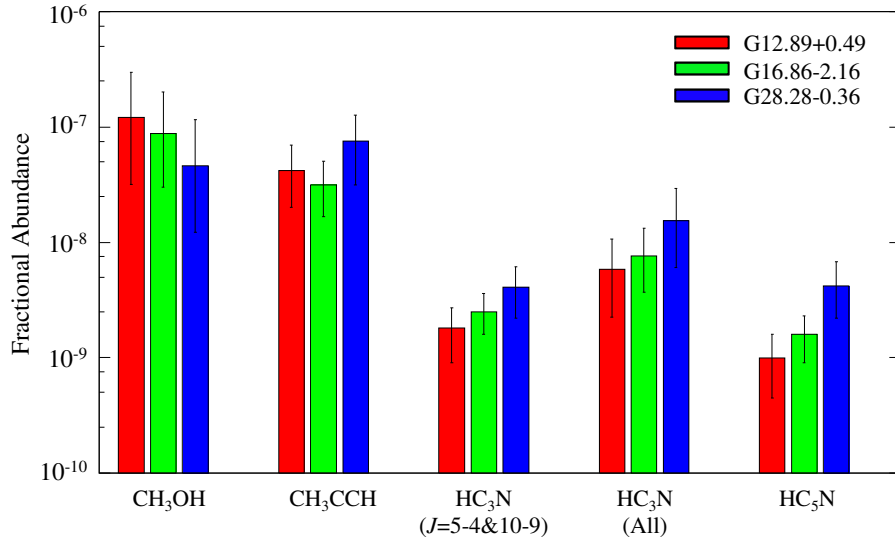


**Figure 8.** Fractional abundances of CH<sub>3</sub>OH, CH<sub>3</sub>CCH, HC<sub>3</sub>N, and HC<sub>5</sub>N in the high-mass star-forming regions. The HC<sub>5</sub>N values are taken from Taniguchi et al. (2017b).

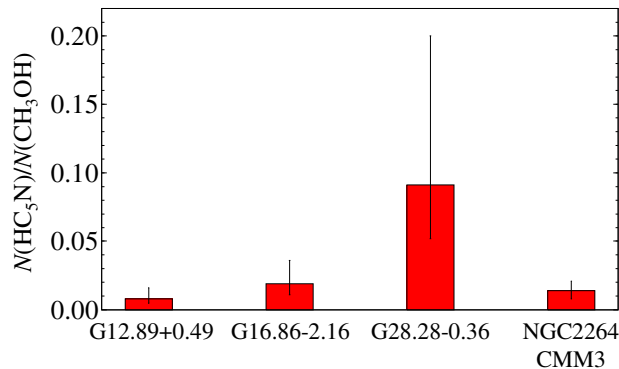


**Figure 9.** Comparison of the  $N(\text{HC}_5\text{N})/N(\text{CH}_3\text{OH})$  ratio among the three high-mass star-forming regions. The data for NGC2264 CMM3 were taken from Watanabe et al. (2015).

Our source sample was chosen from the HC<sub>5</sub>N-detected source list by Green et al. (2014). HC<sub>5</sub>N was not detected in more than half of the sources where Green et al. (2014) carried out observations. In addition, Taniguchi et al. (2018) detected HC<sub>5</sub>N in half of high-mass protostellar objects in their source list. The  $N(\text{HC}_5\text{N})/N(\text{CH}_3\text{OH})$  ratio should cover a broader range of values than the presented here, when considering the HC<sub>5</sub>N-undetected sources into consideration.

### 5.3. Relationship between $N(\text{HC}_5\text{N})/N(\text{CH}_3\text{OH})$ and $N(\text{CH}_3\text{CCH})/N(\text{CH}_3\text{OH})$

In this subsection, we follow the analysis by Fayolle et al. (2015) who compared the chemical composition normalized by CH<sub>3</sub>OH among MYSOs. We compare the chemical composition in the lukewarm envelope using the  $N(\text{HC}_5\text{N})/N(\text{CH}_3\text{OH})$  and  $N(\text{CH}_3\text{CCH})/N(\text{CH}_3\text{OH})$  ratios.

Figure 10 shows the relationship between the  $N(\text{HC}_5\text{N})/N(\text{CH}_3\text{OH})$  ratio and  $N(\text{CH}_3\text{CCH})/N(\text{CH}_3\text{OH})$  ratio in the four MYSOs, the observed three sources and NGC2264 CMM3 (Watanabe et al. 2015). The  $N(\text{HC}_5\text{N})/N(\text{CH}_3\text{OH})$  ratio correlates with the  $N(\text{CH}_3\text{CCH})/N(\text{CH}_3\text{OH})$  ratio. This is caused by the fraction of the lukewarm envelope in the single-dish beams, rather than the chemical differentiation. The chemical composition, based on HC<sub>5</sub>N and CH<sub>3</sub>CCH, of the lukewarm gas in G28.28–0.36 is similar to those in G16.86–2.16 and NGC2264 CMM3 (Ratio ~ 20). On the other hand, the  $N(\text{CH}_3\text{CCH})/N(\text{CH}_3\text{OH})$  ratio compared to the  $N(\text{HC}_5\text{N})/N(\text{CH}_3\text{OH})$  ratio in G12.89+0.49

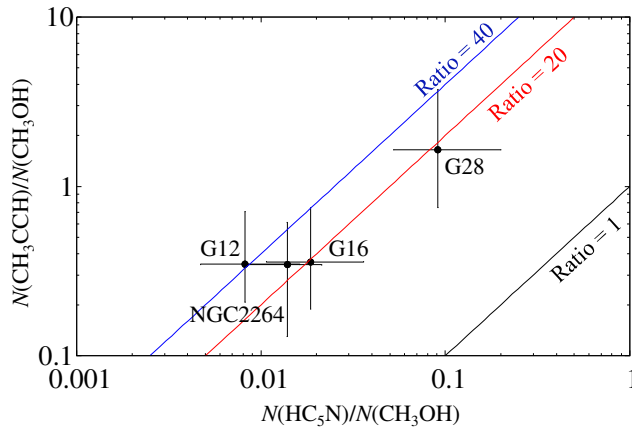


**Figure 10.** Plot of  $N(\text{CH}_3\text{CCH})/N(\text{CH}_3\text{OH})$  versus  $N(\text{HC}_5\text{N})/N(\text{CH}_3\text{OH})$ . The data for NGC2264 CMM3 were taken from Watanabe et al. (2015). The labels of G12, G16, G28, and NGC2264 indicate the plots for G12.89+0.49, G16.86–2.16, G28.28–0.36, and NGC2264 CMM3, respectively.

is higher (Ratio  $\approx 40$ ) than those in the other three sources. These results suggest the chemical diversity in the lukewarm envelope.

#### 5.4. Relationship of the Chemical Composition between Central Core and Envelope

He et al. (2012) carried out 1-mm spectral line survey observations toward 89 GLIMPSE Extended Green Objects (EGOs; Cyganowski et al. 2008). From their survey observations, there are largely two types of EGO clouds; line-rich and line-poor sources. It is unclear why some sources show line-poor spectra, and others show many lines of COMs. Ge et al. (2014) suggested that the EGO cloud cores are possibly in the short onset phase of the hot core stage, when  $\text{CH}_3\text{OH}$  ice is quickly evaporating from grain surfaces at a gas temperature of  $\sim 100$  K. Hence, the difference between the line-poor and line-rich EGO cloud cores seems to originate from the chemical differentiation rather than the chemical evolution. Besides, Fayolle et al. (2015) compared the chemistry between organic-poor MYSOs and organic-rich MYSOs, namely hot cores, but the relationship between the central core and the envelope was not clear. In this subsection, we discuss a possibility of the relationship of the chemical composition between the core and the envelope.

There are clear differences in the spectra among the three sources (Figures 4 – 6). As summarized in Table 6, the detected COMs are different among the three observed sources.  $\text{CH}_3\text{CHO}$  was detected toward all of the three sources, and it is considered to exist in the envelope (Fayolle et al. 2015). In G12.89+0.49, the largest number of COMs have been detected, while G28.28–0.36 is a line-poor source. The results in G28.28–0.36, a line-poor source, are consistent with those of He et al. (2012), showing that only  $\text{H}^{13}\text{CO}^+$  was detected in G28.28–0.36. As discussed in Section 5.2, the  $N(\text{HC}_5\text{N})/N(\text{CH}_3\text{OH})$  ratio in G28.28–0.36 is higher than that in G12.89+0.49 by an order of magnitude. In the case of G16.86–2.16, the  $N(\text{HC}_5\text{N})/N(\text{CH}_3\text{OH})$  ratio shows a value between G12.89+0.49 and G28.28–0.36, and the line density and the COM’s line intensities are also between the others. From these results, the line-poor MYSOs are likely to be surrounded by the carbon-chain-rich envelope, while the line-rich MYSOs, namely hot cores, appear to be surrounded by the  $\text{CH}_3\text{OH}$ -rich envelope.

#### 5.5. Isotopic Fractionation of $\text{HC}_3\text{N}$

The  $^{12}\text{C}/^{13}\text{C}$  ratio shows a gradient with distance from the Galactic center ( $D_{\text{GC}}$ ; e.g., Savage et al. 2002; Milam et al. 2005). Recent observations derived the following relationship (Halfen et al. 2017);

$$^{12}\text{C}/^{13}\text{C} = 5.21(\pm 0.52)D_{\text{GC}} + 22.6(\pm 3.3), \quad (5)$$

where  $D_{\text{GC}}$  is in units of kpc. We estimated the  $D_{\text{GC}}$  values of each source using trigonometry. The  $D_{\text{GC}}$  values are estimated at 5.8 and 8.9 kpc for G12.89+0.49 and G16.86–2.16, respectively. The  $D_{\text{GC}}$  value of G28.28–0.36 was derived to be 5.4 kpc by Taniguchi et al. (2016b). From Equation (5), the  $^{12}\text{C}/^{13}\text{C}$  ratios are calculated at  $53 \pm 6$ ,  $69 \pm 8$ , and  $51 \pm 6$  in G12.89+0.49, G16.86–2.16, and G28.28–0.36, respectively.

The  $^{12}\text{C}/^{13}\text{C}$  ratios derived from observations (Table 9) are generally lower than or consistent with the values calculated from Equation (5) within the errors, except for non-detection species. These results mean that the  $^{13}\text{C}$  species of  $\text{HC}_3\text{N}$  are not heavily diluted. The  $^{12}\text{C}/^{13}\text{C}$  ratios of cyanopolyynes in dark clouds (e.g., TMC-1, L1521B, and L134N; Taniguchi et al. 2016a, 2017a) are generally lower than those of other carbon-chain species (e.g., CCH, CCS,  $\text{C}_3\text{S}$ ,  $\text{C}_4\text{H}$ ), which means that the  $^{13}\text{C}$  species of cyanopolyynes are not heavily diluted. Similar results with the  $^{12}\text{C}/^{13}\text{C}$  ratios of  $\text{HC}_3\text{N}$  being not significantly high were also found in the warm gas around the protostar L1527 (Taniguchi et al. 2016b). Our results show the similar tendency to the local low-mass star-forming regions.

Belloche et al. (2016) reported a tentative detection of  $\text{DC}_3\text{N}$  toward the Sgr B2 (N2) hot core and derived the D/H ratio to be 0.09%. A tentative detection of  $\text{DC}_3\text{N}$  was also achieved toward the Compact Ridge and the hot core of Orion KL (Esplugues et al. 2013), and the deuterium fractionation was estimated at  $1.5 \pm 0.9\%$ . The deuterium fractionation in the high-mass protostellar object NGC2264 CMM3 was calculated at  $1.8 \pm 1.5\%$  from a tentative detection of  $\text{DC}_3\text{N}$  (Watanabe et al. 2015). The higher D/H values were reported toward cold dense cores (5%–10%, Howe et al. 1994) and toward the L1527 protostar, which is one of the warm carbon chain chemistry sources ( $\sim 3\%$ , Sakai et al. 2009b). The D/H values of  $\text{HC}_3\text{N}$  in G16.86–2.16 and G28.28–0.36 ( $\sim 1 - 5\%$ ) is higher than that in Sgr B2, lower than cold dense cores, and comparable to Orion KL hot core and L1527. On the other hand,  $\text{DC}_3\text{N}$  was not detected in G12.89+0.49 and we only derived the upper limit for its D/H ratio, which is significantly lower than those in G16.86–2.16 and G28.28–0.36. In general, the D/H ratio becomes lower in the higher temperature regions (e.g., Caselli & Ceccarelli 2012). Hence, the results may imply that the emission of  $\text{HC}_3\text{N}$  comes from the G12.89+0.49 central hot core position, and the lukewarm envelope component is less than those in the other two sources. In the observations presented here, the lukewarm envelopes and the central cores were covered by the single-dish beam, and we cannot distinguish between them. The D/H ratio significantly depends on the temperature, and we need the high-spatial resolution observations using interferometers such as ALMA to derive the temperature dependence of the D/H ratio.

### 5.6. A Comparison of Line Width of $\text{CH}_3\text{OH}$

Line width is a key tool to characterize the environments where the molecules exist. In general, high-excitation energy lines are expected to trace the hotter gas and show broad line widths, whereas low-excitation energy lines come mainly from cold molecular clouds and show narrow line widths. We detected several  $\text{CH}_3\text{OH}$  emission lines with different excitation energies. We will investigate the relationship between the excitation energy and the line width of  $\text{CH}_3\text{OH}$  in this subsection.

Figure 11 shows a comparison between the line widths of  $\text{CH}_3\text{OH}$  and the excitation energy of each line. We derive the line width ( $\Delta v$ ) using the following formula;

$$\Delta v = \sqrt{\Delta v_{\text{obs}}^2 - \Delta v_{\text{inst}}^2}, \quad (6)$$

where  $\Delta v_{\text{obs}}$  and  $\Delta v_{\text{inst}}$  are the observed line widths (Tables 5 and 7) and the instrumental velocity width ( $0.85 \text{ km s}^{-1} - 0.86 \text{ km s}^{-1}$ , Section 2), respectively.

We conducted the Kendall's  $\tau$  correlation coefficient test. The probability ( $p$ ) that there is no correlation between the line width and the excitation energy is calculated at 0.03%, and the  $\tau$  value is +0.51 in G12.89+0.49. This suggests the weak positive correlation between the line width and the excitation energy. The  $p$  and  $\tau$  values are derived to be 69% and +0.08 in G16.86–2.16, respectively. In G28.28–0.36, the  $p$  and  $\tau$  values are 72% and  $-0.45$ , respectively. Hence, there is no clear correlation between the line width and the excitation energy in G16.86–2.16 and G28.28–0.36. This may be caused by the non-detection of the very-high-excitation energy lines in the two sources.

We also compared the distributions of the  $\text{CH}_3\text{OH}$  line widths among the three sources using the two-sample Kolmogorov-Smirnov test (K-S test). We compared the distributions for all of the combinations; (a) G12.89+0.49 and G28.28–0.36, (b) G16.86–2.16 and G28.28–0.36, and (c) G12.89+0.49 and G16.86–2.16. The probabilities that the distributions of the line widths in the selected two sources are the same are derived to be  $3.2 \times 10^{-4}\%$ ,  $5.8 \times 10^{-3}\%$ , and 39% for case (a), (b), and (c), respectively. These results mean that the distribution of the  $\text{CH}_3\text{OH}$  line width in G28.28–0.36 is clearly different from those in the other two sources, and we cannot exclude the possibility that the distributions in G12.89+0.49 and G16.86–2.16 are different.

The average line widths of  $\text{CH}_3\text{OH}$  are  $4.8 \pm 0.6$ ,  $5.2 \pm 0.6$ , and  $2.6 \pm 0.5 \text{ km s}^{-1}$  in G12.89+0.49, G16.86–2.16, and G28.28–0.36, respectively. Although the average line widths in G12.89+0.49 and G16.86–2.16 are consistent with each other within the errors, G16.86–2.16 shows the highest value; nevertheless the very-high-excitation energy

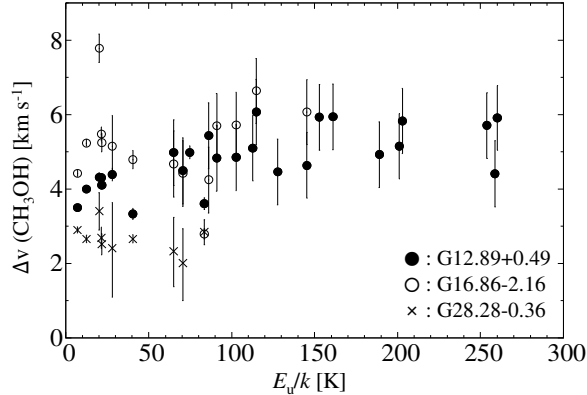


**Figure 11.** Relationship between excitation energy and line width of  $\text{CH}_3\text{OH}$ .

lines were not detected in G16.86–2.16. These imply that  $\text{CH}_3\text{OH}$  exists in turbulent gas such as a molecular outflow in G16.86–2.16 rather than the hot gas. This is supported by the strong wing emission in the  $\text{CH}_3\text{OH}$  spectra in G16.86–2.16. In G12.89+0.49,  $\text{CH}_3\text{OH}$  seems to exist in the hot gas as well as in molecular outflow suggested by the wing emission. On the other hand, the line width in G28.28–0.36 is much narrower than those in the other two sources. This suggests that  $\text{CH}_3\text{OH}$  exists mainly in the relatively quiescent region, i.e. envelope for this source. The non-detection of the very-high-excitation energy lines is consistent with the envelope origin. There is a possibility of the molecular outflow origin, but a low S/N ratio prevents us from confirmation.

## 6. CONCLUSIONS

We carried out observations in the 42–46 and 82–103 GHz bands with the Nobeyama 45-m radio telescope, and in the 338.2–339.2 and 348.45–349.45 GHz bands with the ASTE 10-m telescope toward the three high-mass star-forming regions associated with the 6.7 GHz  $\text{CH}_3\text{OH}$  masers, G12.89+0.49, G16.86–2.16, and G28.28–0.36. The rotational temperatures and the beam-averaged column densities of  $\text{HC}_5\text{N}$ ,  $\text{CH}_3\text{CCH}$ , and  $\text{CH}_3\text{OH}$  in the three sources are derived.

The  $N(\text{HC}_5\text{N})/N(\text{CH}_3\text{OH})$  ratio in G28.28–0.36 is higher than that in G12.89+0.49 by one order of magnitude and that in G16.86–2.16 by a factor of 5. Moreover, the relationships between the  $N(\text{HC}_5\text{N})/N(\text{CH}_3\text{OH})$  ratio and the  $N(\text{CH}_3\text{CCH})/N(\text{CH}_3\text{OH})$  ratio in G28.28–0.36 and G16.86–2.16 are similar to each other, while  $\text{HC}_5\text{N}$  is deficient when compared to  $\text{CH}_3\text{CCH}$  in G12.89+0.49. These results may imply the chemical diversity of the lukewarm envelope.

The line density in G28.28–0.36 is significantly low and a few COMs have been detected, while oxygen-/nitrogen-bearing COMs and high-excitation-energy lines have been detected from G12.89+0.49. These results seem to imply that the organic-poor MYSOs (G28.28-0.36) are surrounded by the carbon-chain-rich lukewarm envelope, whereas the organic-rich MYSOs (G12.89+0.49 and G16.86-2.16), hot cores, are surrounded by the  $\text{CH}_3\text{OH}$ -rich lukewarm envelope. The results presented in this paper were led based on observations with single-dish telescopes without information about the spatial distributions of each molecular emission and only a few molecular species. Further observations are required to confirm the trends reported in this work.

We thank the anonymous referee who gave us valuable comments which helped us improve the quality of this paper. We would like to express our great thanks to the members of the Nobeyama Radio Observatory. The Nobeyama Radio Observatory is a branch of the National Astronomical Observatory of Japan (NAOJ), National Institutes of Natural Sciences. The Z45 receiver is supported in part by a Granting-Aid for Science Research of Japan (24244017). We thank to the operation staff members of the ASTE. The ASTE telescope is operated by the NAOJ. KT appreciates support from a Granting-Aid for Science Research of Japan (17J03516). LM also acknowledges support from the NASA postdoctoral program. A portion of this research was carried out at the Jet Propulsion Laboratory, California Institute of Technology, under a contract with the National Aeronautics and Space Administration.

*Facilities:* Nobeyama 45-m radio telescope, Atacama Submillimeter Telescope Experiment (ASTE)



*Software:* JavaNEWSTAR (<https://www.nro.nao.ac.jp/nro45mrt/html/obs/newstar/index.html>)

## REFERENCES

- Aikawa, Y., Wakelam, V., Garrod, R. T., & Herbst, E. 2008, *ApJ*, 674, 993
- Bacmann, A., Taquet, V., Faure, A., Kahane, C., & Ceccarelli, C. 2012, *A&A*, 541, L12
- Balucani, N., Ceccarelli, C., & Taquet, V. 2015, *MNRAS*, 449, L16
- Belloche, A., Müller, H. S. P., Garrod, R. T., & Menten, K. M. 2016, *A&A*, 587, A91
- Bisschop, S. E., Jørgensen, J. K., van Dishoeck, E. F., & de Wachter, E. B. M. 2007, *A&A*, 465, 913
- Caselli, P., & Ceccarelli, C. 2012, *A&A Rv*, 20, 56
- Cernicharo, J., Marcelino, N., Roueff, E., et al. 2012, *ApJL*, 759, L43
- Chapman, J. F., Millar, T. J., Wardle, M., Burton, M. G., & Walsh, A. J. 2009, *MNRAS*, 394, 221
- Cyganowski, C. J., Whitney, B. A., Holden, E., et al. 2008, *AJ*, 136, 2391
- Esplugues, G. B., Cernicharo, J., Viti, S., et al. 2013, *A&A*, 559, A51
- Fayolle, E. C., Öberg, K. I., Garrod, R. T., van Dishoeck, E. F., & Bisschop, S. E. 2015, *A&A*, 576, A45
- Garrod, R. T., Wakelam, V., & Herbst, E. 2007, *A&A*, 467, 1103
- Ge, J. X., He, J. H., Chen, X., & Takahashi, S. 2014, *MNRAS*, 445, 1170
- Goldsmith, P. F., & Langer, W. D. 1999, *ApJ*, 517, 209
- Green, C. -E., Green, J. A., Burton, M. G., et al. 2014, *MNRAS*, 443, 2252
- Halfen, D. T., Woolf, N. J., & Ziurys, L. M. 2017, *ApJ*, 845, 158
- Hasegawa, T. I., & Herbst, E. 1993, *MNRAS*, 261, 83
- Hassel, G. E., Herbst, E., & Garrod, R. T. 2008, *ApJ*, 681, 1385
- He, J. H., Takahashi, S., & Chen, X. 2012, *ApJS*, 202, 1
- Herbst, E., & van Dishoeck, E. F. 2009, *ARA&A*, 47, 427
- Hirota, T., M. Ohishi, & Yamamoto, S. 2009, *ApJ*, 699, 585
- Howe, D. A., Millar, T. J., Schilke, P., & Walmsley, C. M. 1994, *MNRAS*, 267, 59
- Iguchi, S., & Okuda, T. 2008, *PASJ*, 60, 857
- Imai, M., Sakai, N., Oya, Y., et al. 2016, *ApJL*, 830, L37
- Jaber, A. A., Ceccarelli, C., Kahane, C., & Caux, E. 2014, *ApJ*, 791, 29
- Kamazaki, T., Okumura, S. K., Chikada, Y., et al. 2012, *PASJ*, 64, 29
- Lahuis, F., & van Dishoeck, E. F. 2000, *A&A*, 355, 699
- Li, F. C., Xu, Y., Wu, Y. W., et al. 2016, *AJ*, 152, 92
- Majumdar, L., Gratier, P., Andron, I., Wakelam, V., & Caux, E. 2017a, *MNRAS*, 467, 3525
- Majumdar, L., Gratier, P., Ruaud, M., et al. 2017b, *MNRAS*, 466, 4470
- Majumdar, L., Gratier, P., Vidal, T., et al. 2016, *MNRAS*, 458, 1859
- Marcelino, N., Cernicharo, J., Agúndez, M., et al. 2007, *ApJL*, 665, L127
- Milam, S. N., Savage, C., Brewster, M. A., Ziurys, L. M., & Wyckoff, S. 2005, *ApJ*, 634, 1126
- Müller, H. S. P., Schlöder, F., Stutzki, J., & Winnewisser, G. 2005, *JMoSt*, 742, 215
- Nakajima, T., Kimura, K., Nishimura, A., et al. 2013, *PASP*, 125, 252
- Nakamura, F., Ogawa, H., Yonekura, Y., et al. 2015, *PASJ*, 67, 117
- Öberg, K. I., Bottinelli, S., Jørgensen, J. K., & van Dishoeck, E. F. 2010, *ApJ*, 716, 825
- Okuda, T., & Iguchi, S. 2008, *PASJ*, 60, 315
- Potapov, A., Sánchez-Monge, Á., Schilke, P., et al. 2016, *A&A*, 594, A117
- Purcell, C. R., Balasubramanyam, R., Burton, M. G., et al. 2006, *MNRAS*, 367, 553
- Purcell, C. R., Longmore, S. N., Burton, M. G., et al. 2009, *MNRAS*, 394, 323
- Reboussin, L., Wakelam, V., Guilloteau, S., & Hersant, F. 2014, *MNRAS*, 440, 3557
- Reid, M. J., Menten, K. M., Brunthaler, A., et al. 2014, *ApJ*, 783, 130
- Ruaud, M., Wakelam, V., & Hersant, F. 2016, *MNRAS*, 459, 3756
- Sakai, N., Sakai, T., Hirota, T., Burton, M., & Yamamoto, S. 2009a, *ApJ*, 697, 769
- Sakai, N., Sakai, T., Hirota, T., & Yamamoto, S. 2008, *ApJ*, 672, 371-381
- Sakai, N., Sakai, T., Hirota, T., & Yamamoto, S. 2009b, *ApJ*, 702, 1025
- Savage, C., Apponi, A. J., Ziurys, L. M., & Wyckoff, S. 2002, *ApJ*, 578, 211
- Shimajiri, Y., Sakai, T., Kitamura, Y., et al. 2015, *ApJS*, 221, 31
- Suzuki, H., Yamamoto, S., Ohishi, M., et al. 1992, *ApJ*, 392, 551
- Taniguchi, K., Ozeki, H., & Saito, M. 2017a, *ApJ*, 846, 46
- Taniguchi, K., Ozeki, H., Saito, M., et al. 2016a, *ApJ*, 817, 147

- Taniguchi, K., Saito, M., Hirota, T., et al. 2017b, *ApJ*, 844, 68
- Taniguchi, K., Saito, M., & Ozeki, H. 2016b, *ApJ*, 830, 106
- Taniguchi, K., Saito, M., Sridharan, T. K., & Minamidani, T. 2018, *ApJ*, 854, 133
- Tielens, A. G. G. M., & Hagen, W. 1982, *A&A*, 114, 245
- Urquhart, J. S., Moore, T. J. T., Schuller, F., et al. 2013, *MNRAS*, 431, 1752
- van Dishoeck, E. F. 2017, arXiv:1710.05940
- Vastel, C., Ceccarelli, C., Lefloch, B., & Bachiller, R. 2014, *ApJL*, 795, L2
- Watanabe, Y., Sakai, N., López-Sepulcre, A., et al. 2015, *ApJ*, 809, 162